Confinement and Kink Entanglement Asymmetry on a Quantum Ising Chain

B. J. J. Khor[1,2], D.M. Kürkçüoğlu[2,3], T. J. Hobbs[4], G. N. Perdue[2], and I. Klich[1]

[1]Department of Physics, University of Virginia, Charlottesville, VA, USA

[2]Fermi National Accelerator Laboratory, Batavia, IL 60510, USA

[3]Superconducting Quantum Materials and Systems Center (SQMS), Fermi National Accelerator Laboratory, Batavia, IL 60510, USA

[4]High Energy Physics Division, Argonne National Laboratory, Argonne, IL 60439, USA

In this work, we explore the interplay of confinement, string breaking and entanglement asymmetry on a 1D quantum Ising chain. We consider the evolution of an initial domain wall and show that, surprisingly, while the introduction of confinement through a longitudinal field typically suppresses entanglement, it can also serve to increase it beyond a bound set for free particles. Our model can be tuned to conserve the number of domain walls, which gives an opportunity to explore entanglement asymmetry associated with link variables. We study two approaches to deal with the non-locality of the link variables, either directly or following a Kramers-Wannier transformation that maps bond variables (kinks) to site variables (spins). We develop a numerical procedure for computing the asymmetry using tensor network methods and use it to demonstrate the different types of entanglement and entanglement asymmetry.

1 Introduction

Strongly-coupled theories such as QCD can possess rich structure-forming properties relevant to many domains in modern physics. Despite advances in nonperturbative methods like lattice gauge theory and phenomenological modeling, a thorough understanding of QCD remains elusive due to the phenomenon of confinement [65]. Recently, entanglement entropy has been suggested as providing a theoretical tool to investigate QCD systems, both in terms of bound states [19, 30, 36] and with respect to scattering processes [1, 6, 13, 15, 39].

In parallel, quantum spin chains have been proposed as analogous systems to investigate confinement analytically and numerically [8, 18, 41, 50, 53, 54, 62]. In particular, the Ising spin chain has been a useful setup to study confinement in real time [33]. Here, a two-fermion system is represented by domain walls, with binding effects introduced via a longitudinal field that gives an energy penalty linearly proportional to the length of the domain wall [16, 66, 67]. This configuration simulates key aspects of the confinement of quark-antiquark pairs into mesons, or the binding of two-nucleon systems into the deuteron. This simple model, demonstrating confinement in non-equilibrium quantum quench dynamics, has led to an avalanche of related theoretical works [5, 14, 28, 29, 32, 34, 35, 37, 38, 40, 42, 49, 52, 55, 57, 58], and the Ising chain confinement was also recently realized on IBM's quantum hardware [56, 62].

The theory of many-body quantum entanglement can shed insights into confinement and symmetry breaking. Indeed, signatures of confinement show up in entanglement dynamics, where the entanglement entropy is greatly suppressed upon the introduction of the confining field [33, 55, 62]. Symmetry breaking can also manifest in measures of entanglement entropy. When a wave function possesses a local symmetry, its entanglement entropy is a statistical combination of entropies associated to each local occupation number sector [4, 17, 31]. When a local symmetry is broken, however, additional contributions to entropy are generated and can be quantified using "entanglement asymmetry" [2, 3, 11, 21]. Various measures of symmetry-resolved entropy have been explored [9, 25, 43–46, 51, 61, 61].

B. J. J. Khor: bk8wj@virginia.edu

D.M. Kürkçüoğlu: dogak@fnal.gov

T. J. Hobbs: tim@anl.gov

G. N. Perdue: perdue@fnal.gov

I. Klich: klich@virginia.edu

2 Model and Entanglement Measures

In this paper, we study the nature of meson dynamics through the lens of entanglement entropy and its

asymmetry. In particular, we address the questions: is entropy always suppressed by a confining field? How can one address entanglement asymmetry for a quasi-local conservation law? To do so, we consider the Ising model with transverse and longitudinal fields and an additional three-body term that can be tuned to render the dynamics meson-number conserving for special points in parameter space [24, 27]:

$$H = -J_0 \sum_{i=1}^{L-1} \sigma_i^z \sigma_{i+1}^z - g \sum_{i=2}^{L-1} \sigma_i^x - h \sum_{i=1}^{L} \sigma_i^z - J \sum_{i=1}^{L-2} \sigma_i^z \sigma_{i+1}^x \sigma_{i+2}^z \cdot \tag{1}$$

This model exhibits confinement in the spreading of meson (kink/anti-kink pair) excitations for nonzero longitudinal fields, $h \neq 0$ [42, 62, 63]. When we set $J = -g$, the model is dual to a fermionic chain coupled with a $\mathbb{Z}_2$ gauge theory [10]; it is kink-number preserving and exhibits quantum many body scars [24, 26, 27]. We further note that the three-body term in the kink preserving regime naturally appears in applications such as the anti-blockade regime of the Rydberg simulators [48], and that quantum many-body scar eigenstates of the kink preserving model have been prepared on IBM superconducting hardware [26].

The Hamiltonian (1) can be mapped to a fermionic model using a combination of Kramers-Wannier and Jordan-Wigner transformations (see Appendix E):

$$\begin{aligned} H &= -2J_0 \sum_{j=2}^{L} c_j^\dagger c_j - (g-J) \sum_{j=2}^{L-1} (c_j^\dagger c_{j+1} + h.c.) \\ &\quad - (g+J) \sum_{j=2}^{L-1} (c_j^\dagger c_{j+1}^\dagger + h.c.) - h \sum_{j=1}^{L} \prod_{i=1}^{j} \left(2c_i^\dagger c_i - 1 \right) \end{aligned} \tag{2}$$

Here $c_j^\dagger$ are fermion creation operators associated with creating a kink between site j and $j-1$ in the original model. Eq. (2) shows that indeed kink-number preservation is exact for $J = -g$, allowing us to study regimes away from small g, J. On the other hand, when $g \neq -J$, only the kink-number parity is conserved. Throughout the rest of the paper we set $J_0 = 1, \hbar = 1$, thus time scales throughout this paper are set in the unit of J_0^{-1}.

We consider the time evolution of an initial domain wall product state of length n, i.e., of the form

$$|j, n\rangle \equiv |\ldots \uparrow\downarrow_j \ldots \downarrow_{j+n-1}\uparrow \ldots\rangle \,. \tag{3}$$

Entanglement can be quantified via Rényi entropies,

$$S_n(\rho_A) = \log_2(\text{Tr}(\rho_A^n))/(1-n) \,, \tag{4}$$

where $\rho_A = \text{Tr}_B \rho$ is a reduced density matrix associated with a subset of sites A when its complement, B, has

been integrated out. In particular, the second-order Rényi entropy is $S_2(\rho_A) = -\log_2 \text{Tr}(\rho_A^2)$.

We evaluate $S_2(\rho_A)$ in numerical simulations below. Within time-evolving block decimation (TEBD) [59, 60, 64], this generalizes to other entropy orders. Another quantity of interest is the kink density, $\Delta_{i,i+1}^{zz} \equiv \frac{1}{2}\langle(1 - \sigma_i^z \sigma_{i+1}^z)\rangle$, with $\Delta_{i,i+1}^{zz} = 1\,(0)$ for a spin flip (alignment).

3 Kink-preserving Dynamics

As mentioned, with the choice $J = -g$, the Hamiltonian in Eq. (1) preserves kink number. To study the evolution of a kink, we project H onto the two-kink subspace in the kink basis, Eq. (3):

$$\begin{aligned} H_2 &= \sum_{\substack{0 \leq j < L-1 \\ 0 < n < L-j-1}} 2hn|j, n\rangle\langle j, n| - (g-J)\Big(|j-1, n+1\rangle + \\ &\quad |j+1, n-1\rangle + |j, n-1\rangle + |j, n+1\rangle\Big)\langle j, n| \,. \end{aligned} \tag{5}$$

This projection is exact when H conserves kink number. Eq. (5) highlights an advantage of adding the three body term in controlling kink production compared to working without the three body interaction $\sigma_i^z \sigma_{i+1}^x \sigma_{i+2}^z$ modification of the transverse field Ising, while assuming g is small. Indeed in the later case, kinks appear perturbatively on the background of a classical Ising chain and propagate slowly, since their kinetics is governed by g. Including the three body term, Eq. (5) shows that the dynamics of the two kink bound states (with $g = -J$) is characterized by the kinetic energy scale $g - J$, which can be tuned to be arbitrarily large, allowing us to study regimes of fast dynamics while preserving kink number.

We note that the exactness of H_2 offers an opportunity to benchmark tensor network methods against the corresponding computation by exact evolution in the two-kink subspace. In particular, we compare the evolution of the local kink density, as well as the 2nd Rényi entropy as computed by exact diagonalization within the two-kink subspace with corresponding computations within TEBD evolution. Interestingly, we are not aware of any previous calculation of Rényi entropy directly in the two-kink subspace Hamiltonian in Eq. (5), and we outline the computational approach in Appendix B. We also verify the validity of the two-kink subspace dynamics by comparing the time evolution for various observables and the Rényi entropy with identical quantities computed from small-size exact diagonalization in Appendix A.
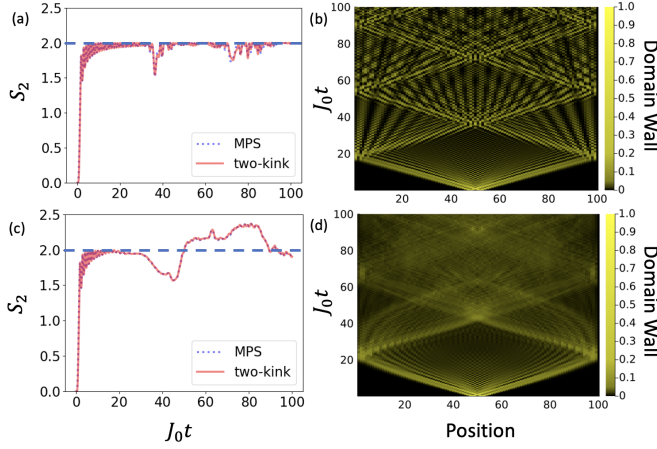
Figure 1: Evolution of half chain Rényi entropy for (a) $g = -J = 0.7, h = 0$ and (c) $g = -J = 0.7, h = 0.05$. The corresponding domain wall profile following a quench are (b) $g = -J = 0.7, h = 0$ and (d) $g = -J = 0.7, h = 0.05$ respectively. The initial state $|\uparrow \ldots \uparrow\downarrow\downarrow\downarrow\downarrow\uparrow \ldots \uparrow\rangle$ is $L = 100$ spin chain with $n = 4$ initial domain size in the middle of the spin chain.
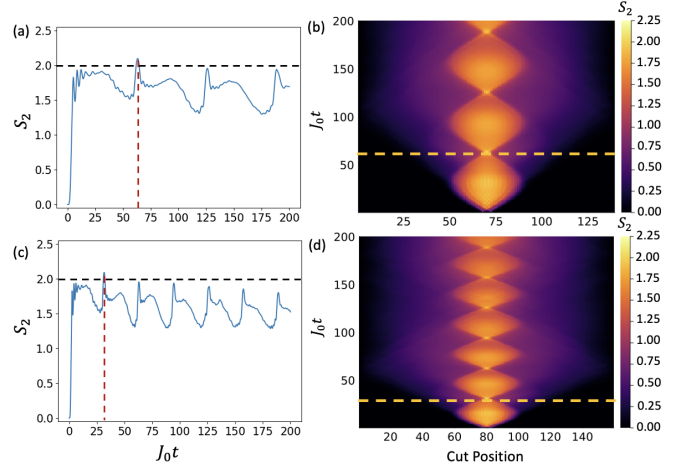

Figure 2: Half chain Rényi entropy for (a) $g = -J = 0.25, h = 0.05, L = 140$ and (c) $g = -J = 0.5, h = 0.1, L = 160$. The right figures are bipartite Rényi entropy at all possible cuts along the chain for (b) $g = -J = 0.25, h = 0.05, L = 140$ and (d) $g = -J = 0.5, h = 0.1, L = 160$, for which the left figures are only a slice along the middle of the spin chain. The initial states $|\uparrow \ldots \uparrow\downarrow\downarrow\downarrow\downarrow\uparrow \ldots \uparrow\rangle$ has $n = 4$ initial domain size in the middle of the spin chain of size of either $L = 140$ or $L = 160$. See Appendix C for accompanying kink density plot.

4 Rényi Entropy saturation, integrability and confinement

In Fig. 1, we consider the evolution of an initially small domain, focusing on the half-chain entropy, $S_2(t)$, and on the kink density. Note the remarkable agreement between the exact diagonalization and TEBD computations, validating the TEBD approach, at least for small kink numbers.

A striking feature of the Rényi entropy dynamics in Fig. 1 (a) is that when $h = 0$ and $g = -J$, the second-order Rényi entropy saturates at $S_2 \leq 2$ when we set our initial state to be a two-kink state. This is surprising at first since a generic two-kink wave function can have a much larger entropy, up to $\log_2(L/2 + 2)$. In Appendix F, we prove that if $h = 0$, and given an initial two-kink state, we have $S_2 \leq 2$ when kink number is conserved.

This bound can be roughly understood as follows. An initial domain wall state (3) corresponds, in the fermion formulation (2), to two initially localized fermions

$$c_j^\dagger c_{j+n}^\dagger |\text{vac}\rangle. \tag{6}$$

When we take $h = 0, J = -g$, the second line in (2), vanishes leaving us with a free fermion Hamiltonian. The subsequent evolution is of a pair of non-interacting, uncorrelated, fermions. Intuitively, each fermion can contribute at most $S_2 = \log_2(2) = 1$ due to its delocalization in the system. The uncorrelated nature of the fermions then implies $S_2 \leq 2$. A rigorous proof is given in Appendix F.

4.1 The effect of confinement and integrability breaking

What happens when $h > 0$? Naively, one may expect that entropy generation will be decreased, due to the reduction of the spread of the particles.

However, considering Fig. 1 (lower), we encounter a surprise: with a small $h = 0.05$, we find a clear violation of the free-particle ($h=0$) bound. Indeed, the collisions and interactions with $h \neq 0$ do not correspond to non-interacting particles and are not bound by the above argument, as can be seen in the fermionic model (2) where the confining term h gives rise to a highly non-local interaction term, thereby allowing quantum correlations and entanglement to develop. We explore this more closely in Fig. 2. The evolution exhibits the following features: when the string reaches its maximal extent, the entropy starts decreasing, due to a suppression of the wave function spread. However, close to the minimal string size, where collision is possible, entropy shows a rapid increase. When this collision-related increase is sufficient to overcome suppressed entropy, the $S_2 = 2$ bound is violated.

Note that in Fig. 1, the bound violation is enhanced when the size of the chain is smaller than the maximal extent of the wave function spread. In Fig. 2 and the accompanying kink density plot in Appendix C, however, we find that early time collisions can still violate the bound before these boundary effects become

substantial, showing that the bound violation may persist also in the thermodynamic limit, $L \to \infty$. The variations in the Rényi entropy of the system at all cut positions are plotted in the right panels of Fig. 2, showing that the oscillatory behavior of the entropy is reproduced along the internal structure of the meson.
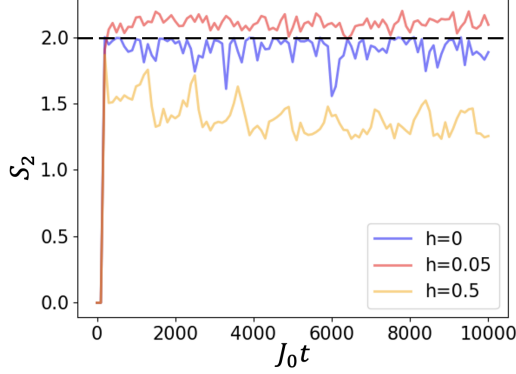

Figure 3: The long time dynamics of the bipartite Rényi entropy $S_2(t)$ from the exact diagonalization of the two-kink Hamiltonian H_2 in Eqn 5. Here, the kink kinetic energy parameter is set to $g = -J = 0.7$, the chain is of length $L = 100$, and we notice that for weak confining field h, the entropy exceeds the $S_2 = 2$ limit while strong confining field h eventually suppresses the entropy growth.

In Fig. 3 we take advantage of the fact that, in exact diagonalization, no Trotterization error is introduced and we can simulate our time evolution dynamics to arbitrarily late times in the exact kink-preserving simulation. Consistent with Fig. 1, when we have $h = 0$, the Rényi entropy is bounded by $S_2 \leq 2$. Upon introducing a small confining field, we see that the Rényi entropy can exceed this upper bound. On the other hand, once the confining field becomes significantly stronger ($h = 0.5$), the Rényi entropy is suppressed compared to the unconfined case, and exhibits oscillatory behavior.

5 Entanglement Asymmetry

We now turn to our second question. What is the effect of symmetry breaking on entanglement entropy when the symmetry operator is not exactly local? Given a local symmetry operator of the form $Q = Q_A \otimes I + I \otimes Q_B$ such as charge or magnetization, a useful quantity utilized to study symmetry breaking and its relation to entanglement entropy is the entanglement asymmetry.

The entanglement asymmetry is obtained as follows. First, we project ρ_A onto the blocks associated with different symmetry sectors of Q_A:

$$\rho_{A,Q} = \sum_q \Pi_q \rho_A \Pi_q \ , \tag{7}$$

where Π_q are projectors onto a subspace with a given eigenvalue q of Q_A. When Q_A has integer eigenvalues, the projected density matrix can be written as

$$\rho_{A,Q} = \int_{-\pi}^{\pi} \frac{d\lambda}{2\pi} e^{-i\lambda Q_A} \rho_A e^{i\lambda Q_A} \ . \tag{8}$$

Then, the projected density matrix can be used to construct the entanglement asymmetry [2], given by

$$\Delta S_n(\rho_A) = S_n(\rho_{A,Q}) - S_n(\rho_A) \ , \tag{9}$$

where $S_n(\rho_{A,Q}) = \log_2 \mathrm{Tr}(\rho_{A,Q}^n)/(1-n)$ is the symmetry-resolved Rényi entropy. The entanglement asymmetry vanishes, $\Delta S_n = 0$, if computed for a state that commutes with Q. A more detailed introduction to entanglement asymmetry is given in, e.g. [2].

5.1 Kink and Kramers-Wannier Entanglement Asymmetries

In contrast to the discussion above and also examples presented in existing literature, we ask the question as to how we can treat entanglement asymmetry when the symmetry operator is not fully local, i.e., the operator associated with the symmetry is not a sum of single site operators.

In our current context, the conservation of kink number is associated with a quasi-local charge (a two-body operator in our case), N_k, since kinks live on the dual lattice, with the number of kinks given by

$$N_k = \sum_{i=1}^{L-1} \Delta_{i,i+1}^{zz} = \frac{1}{2}\left(L - 1 - \sum_{i=1}^{L-1} \langle \sigma_i^z \sigma_{i+1}^z \rangle\right). \tag{10}$$

We break the spin chain into complementary subsystems, A and B, where A contains spins $1, .., L_A$; then,

$$N_k = N_{k,A} \otimes I + I \otimes N_{k,B} + \Delta_{L_A, L_A+1}^{zz} \ , \tag{11}$$

where $N_{k,A}, N_{k,B}$ count the number of kinks within A and its complement B respectively. The last term measures the presence of a kink at the interface between A and B.

The presence of a kink at the interface between A and B is impossible to determine from within subsystem A alone. However, we may compute a coarse-grained entanglement asymmetry by projecting onto blocks with fixed kink number inside A. We define the projected density matrix, $\rho_{A,N_{k,A}}$, as

$$\rho_{A,N_{k,A}} = \int_{-\pi}^{\pi} \frac{d\lambda}{2\pi} e^{-i\lambda N_{k,A}} \rho_A e^{i\lambda N_{k,A}} \ . \tag{12}$$

This projection is depicted schematically in Fig. 4; from this, we define an asymmetry, $\Delta S_2^{kink} \equiv \Delta S_2(\rho_{A,N_{k,A}})$, as in Eq. (9).
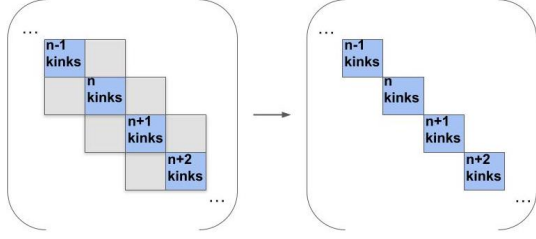

Figure 4: Left: The reduced density matrix ρ_A for an initial wave function with a fixed number of kinks may have terms coupling n kinks in the bulk of A with $n + 1$ or $n - 1$ kinks. Right: the projected matrix $\rho_{A,N_{k,A}}$.

We note that asymmetries computed using $\rho_{A,N_{k,A}}$ may be nonzero even if the overall wave function has a fixed kink number. This is in contrast with the entanglement asymmetry ΔS_n associated with strictly local (one-body) symmetry operator, where ΔS_n necessarily vanishes when the wave function has fixed symmetry eigenvalue. In the case of quasi-local (two-body) kink operator, owing to the presence of the kink at the interface, ΔS_n can be nonzero even when the wave function has fixed kink number.

To see this, consider the example of a very simple wave function:

$$\frac{1}{\sqrt{2}}(|\uparrow\uparrow\downarrow\downarrow\rangle + |\uparrow\downarrow\downarrow\downarrow\rangle), \quad (13)$$

where the first two spin sites define subsystem A, giving:

$$\rho_A = \frac{1}{2}(|\uparrow\uparrow\rangle + |\uparrow\downarrow\rangle)(\langle\uparrow\uparrow| + \langle\uparrow\downarrow|). \quad (14)$$

Note that ρ_A describes a pure state with no entropy, however it is *not* in block form from the point of view of internal kinks in subsystem A. On the other hand

$$\rho_{A,N_{k,A}} = \frac{1}{2}(|\uparrow\uparrow\rangle\langle\uparrow\uparrow| + |\uparrow\downarrow\rangle\langle\uparrow\downarrow|) \quad (15)$$

describes a mixed state with entropy $\log_2 2 = 1$.

Thus our generalized entanglement asymmetry will only vanish for wave functions that have a fixed number of kinks and no kink at the interface between A and B. The presence of kink at the interface, even with fixed kink number, leads to nonzero asymmetry. Nevertheless, the contribution to the asymmetry, ΔS_2^{kink}, from the boundary kink is small: it will be responsible for at most an $O(1)$ contribution to the entropy, and is thus suitable for probing entropy scaling in large systems.

How can we take into account the effect of a possible kink lying at the interface of the bipartition when one calculates quantities such as the entropy? Here, we propose an asymmetry measure that vanishes for eigenstates having total kink number N_k. To do so, we use an open boundary Kramers-Wannier (KW) transformation U_{KW}, which maps $|s_1, ..s_N\rangle \to |t_1, ..t_N\rangle$ where $t_1 = s_1$ and $t_i = s_{i-1}s_i$ for $i > 1$. The Kramers-Wannier transformation maps the link variable (in our case, the kink) to a local site variable, i.e., $\sigma_i^z \sigma_{i+1}^z \to \sigma_{i+1}^z$, and naturally deals with the kink lying in the interface of the bipartition. In particular, U_{KW} maps kink number into magnetization which is completely local, thus in the Kramers-Wannier (KW) basis, the magnetization entanglement asymmetry should vanish for a wave function with a fixed kink number.

Let us consider the relationship between entropies in the original basis vs the KW basis. We take as the set of sites $A = 1, .., L_A$ to be fixed. Given a quantum state on the full system we can define $\rho^{KW} = U_{KW}\rho U_{KW}^\dagger$, and $\rho_A^{KW} = \text{Tr}_B \rho_{KW}$. We show in appendix E that U_{KW} only contains a single two-qubit gate operating between subsystems A, B, and hence $S(\rho_A)$ and $S(\rho_A^{KW})$ differ by at most the entropy that can be generated by such a gate, i.e. at most $2\log_2 2$. Therefore we can use $S(\rho_A^{KW})$ as an alternative measure for questions of entanglement scaling, i.e., whether entropy is bounded when A is large.

Next, let us discuss the transformation of the kink entanglement asymmetry in the original basis into the magnetization entanglement asymmetry in the Kramers-Wannier basis. Note that under U_{KW}, we have $\prod_{i=1}^{l-1} e^{\pm i\lambda \sigma_i^z \sigma_{i+1}^z} \to \prod_{i=2}^{l} e^{\pm i\lambda \sigma_i^z}$ (see Appendix E). Thus, following Eqs. (8),(12), we define the KW projected density matrix as:

$$\rho_{N_k,A}^{KW} = \int_{-\pi}^{\pi} \frac{d\lambda}{2\pi} e^{-i\frac{\lambda}{2}\sum_{l=2}^{L_A} \sigma_l^z} \rho_A^{KW} e^{i\frac{\lambda}{2}\sum_{l=2}^{L_A} \sigma_l^z}, \quad (16)$$

and the KW kink asymmetry as $\Delta S_2^{KW} \equiv S_2(\rho_{N_k,A}^{KW}) - S_2(\rho_A^{KW})$. Note that, ΔS_2^{KW} obeys the desired property that $\Delta S_2^{KW} = 0$ if the system is in a state with a fixed number of kinks. Even in cases when kink number is not conserved in the original basis, we in general expect $\Delta S_2^{KW} \leq \Delta S_2^{kink}$, as the kink entanglement asymmetry in the original basis can miscount a kink lying at the interface [see Eq. (11)].

5.2 MPS implementation

To proceed beyond the kink conserving dynamics we have developed a Matrix Product State (MPS) procedure to compute S_2. Given a local charge of interest (magnetization or $N_{k,A}$) we compute the

asymmetry by expressing $S_2(\rho_{A,Q})$ as

$$S_2(\rho_{A,Q}) = \int_0^{2\pi} \frac{d\lambda}{\pi} \left(1 - \frac{\lambda}{2\pi}\right) \text{Tr}_A[e^{i\lambda Q_A} \rho_A e^{-i\lambda Q_A} \rho_A]. \quad (17)$$

We carry out the trace in Eq. (17) by representing ρ as a matrix product operator and doing the necessary contractions. A discussion of the computational complexity of the procedure is provided in Appendix D.
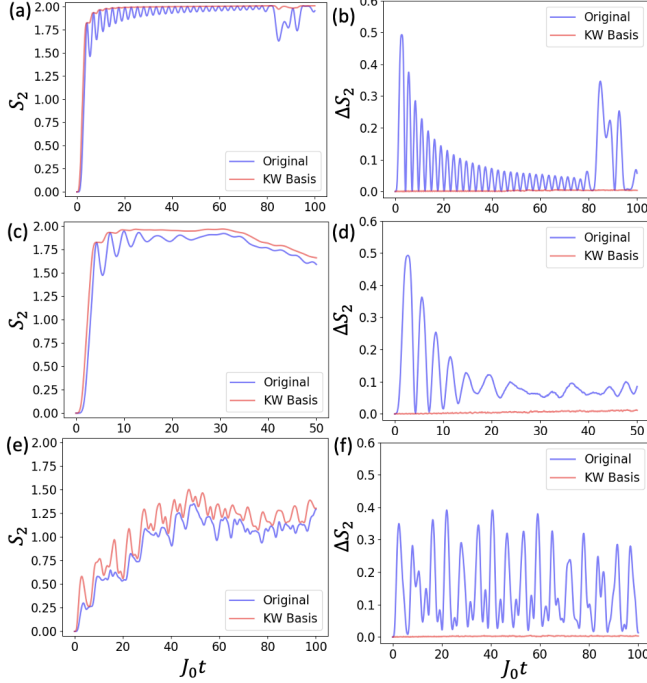

Figure 5: Entropy $S_2(t)$ and asymmetry $\Delta S_2(t)$ for the original basis vs Kramers-Wannier basis. Here, (a) $S_2(t)$ for $h = 0$, (b) $\Delta S_2(t)$ for $h = 0$ (c) $S_2(t)$ for $h = 0.05$, (d) $\Delta S_2(t)$ for $h = 0.05$, (e) $S_2(t)$ for $h = 0.5$, and (f) $\Delta S_2(t)$ for $h = 0.5$. Here, the transverse field and three-body strength are set at $g = 0.3 = -J$ for all figures. The initial states $|\uparrow \ldots \uparrow\downarrow\downarrow\downarrow\downarrow\uparrow \ldots \uparrow\rangle$ for $L = 100$ spin chain has $n = 4$ initial domain size in the middle of the spin chain and the evolution is kink conserving. Note that the shorter time scale of (c) and (d) is due to the higher computational complexity to simulate the Rényi asymmetry for the case $h = 0.05$.

6   Numerical results

We present the numerical results for both the kink-preserving cases and the string breaking cases in Figs. 5 and 6 respectively, in both the original basis and the KW basis, and for Rényi entropy S_2 and Rényi asymmetry ΔS_2. We begin by commenting on the kink-preserving case $g = -J$ in Fig. 5. Note that the
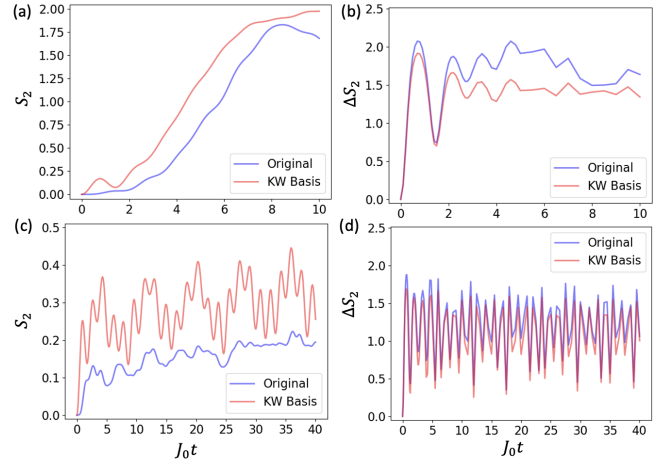

Figure 6: Entropy $S_2(t)$ and asymmetry $\Delta S_2(t)$ in the original vs. the Krammers-Wannier basis.Here, (a) $S_2(t)$ for $h = 0$, (b) $\Delta S_2(t)$ for $h = 0$ (c) $S_2(t)$ for $h = 0.4$ and (d) $\Delta S_2(t)$ for $h = 0.4$. Here, the transverse field and three-body strength are set at $g = 0.4$ and $J = 0.1$ respectively for all figures. The initial states $|\uparrow \ldots \uparrow\downarrow\downarrow\downarrow\downarrow\uparrow \ldots \uparrow\rangle$ for $L = 60$ spin chain has $n = 4$ initial domain size in the middle of the spin chain and the evolution is not kink conserving. Note that the short time scale of the asymmetry evolution owes to the limit of the computational ability to simulate the Rényi asymmetry at later time scales, especially for the $h = 0$ case.

kink Rényi asymmetry ΔS_2^{kink} does not vanish even when the kink number is conserved, consistent with our example illustrated earlier Eq. (13). On the other hand, we verify that in the KW basis the asymmetry ΔS_2^{KW} vanishes, as expected [1].

In Fig. 5, we study three different cases with different confining field strength while keeping the kinetic energy $g = -J$ constant: (1) the free fermion case $h = 0$, (2) weak confinement, $h = 0.05$, and (3) strong confinement $h = 0.5$. We note that $S_2(\rho_A^{KW})$ and $S_2(\rho_A)$ are quite close to each other. Moreover, we observe that $S_2(\rho_A^{KW}) > S_2(\rho_A)$ consistently. We can explain this feature as follows. For weakly correlated states, with low entropy, the wave-function in the vicinity of the cut region is close to a product state in the original basis. As mentioned, the transformation U_{KW} (see appendix E) contains an entangling 2-qubit gate (a CNOT) acting between the sides of the system, which will generically increase the entropy when acting on a weakly correlated state. Thus, we expect that the Rényi entropy S_2 will be enhanced after the Kramers-Wannier transformation compared to the Rényi entropy S_2 in the original basis.

---

[1]Due to the approximate nature of the TEBD time evolution on the MPS, we note that there is error of order 10^{-3} on the kink number conservation, and the magnetization asymmetry error is fluctuating in order of 10^{-3}.

Note the pronounced oscillation of the entropy in the strong confining case. Due to the strong confinement, the kink is oscillating near the entropy cut, which is reflected in large oscillations of the asymmetry in the original basis, while, consistent with our construction, showing that the KW asymmetry vanishes $\Delta S_2^{KW} = 0$ to a good approximation.

Finally, note that the dip in Rényi entropy in the original basis around $t \approx 85$ for $h = 0$ in Fig. 5 is associated with collision of kinks, and is accompanied with a spike in kink asymmetry in the original basis. In general, we observe that dips in S_2 corresponds to spikes in kink asymmetry ΔS_2^{kink}. A kink density heatmap is provided in appendix C (see Fig 11) for reference.

Next we consider kink number violating dynamics in Fig. 6. A common feature shared by the Rényi entropy in the kink-preserving Fig. 5 and string breaking Fig. 6 is that the Rényi entropy in the original basis is in general lower than Rényi entropy in the KW basis.

On the other hand, the kink entanglement asymmetry ΔS_2^{kink} is greater than the KW kink asymmetry ΔS_2^{KW}, though the difference is more pronounced in the kink-preserving case. This behavior may be attributed to the entropy associated with the possibility of a kink at the center of the chain, exactly at the boundary between the left and right regions, as outlined in our discussion in earlier section justifying $\Delta S_2^{KW} \leq \Delta S_2^{kink}$. Comparison with Fig. 5 also shows that, as expected, as soon as kink production is increased, kink-entanglement entropy asymmetry is enhanced. In addition, we see that the KW kink asymmetry ΔS_2^{KW} is in better agreement with ΔS_2^{kink}. This feature can be understood as due to the contribution from possible kinks precisely at the interface playing a less dominant effect.

7 Conclusion and Outlook

In summary, we studied entanglement associated with meson dynamics via confined string evolution and effects of string breaking; we quantified these phenomena through a novel application of entanglement asymmetry in a QCD-analogue model system, a transverse-field Ising chain with three-spin interaction and longitudinal field. We performed the Rényi entropy calculation directly in the two-kink subspace. For kink-preserving dynamics, the absence of a longitudinal field gives rise to integrability that sets an upper bound on Rényi entropy. We find that the dynamics of entanglement production generically involves two stages: when the string is contracting, entropy is reduced, followed by an increase when the minimum size is reached. Turning on the confining field can break the integrability bound with weak confining field. However,

the Rényi entropy is suppressed upon further increasing the strength of the confining field. This calculation reveals the internal dynamics of a simulated bound-state system resembling the meson in QCD through the lens of entanglement entropy.

Another significant aspect of our work is the study of the interplay of entanglement and kink production in the context of entanglement asymmetry. To do so, we introduced the kink entanglement asymmetry and the Kramers-Wannier entanglement asymmetry to address the nature of kink number in our spin chain. To study these numerically, we devised a new calculation of Rényi asymmetry using MPS methods and demonstrated its application in the context of kink entanglement asymmetry.

We comment on a few future directions that are worthy of consideration. A few recent papers [46, 51, 61] explored and proposed measuring entanglement asymmetry in quantum hardware simulations, and it will be interesting to simulate new types of entanglement asymmetry on NISQ devices. In addition, there is a need to develop a more computationally efficient approach to obtain Rényi asymmetry (see e.g. [20]). Addressing this question might allow us to access later time dynamics for Rényi asymmetry, and to see if dynamical purification [61] can be observed in settings similar to our setup. Finally, lattice gauge theories with site and link variables provide natural playgrounds to explore the concept of kink entanglement asymmetry proposed in this work.

References

[1] Yoav Afik and Juan Ramón Muñoz de Nova. Entanglement and quantum tomography with top quarks at the LHC. *The European Physical Journal Plus*, 136(9):907, 2021. DOI: 10.1140/epjp/s13360-021-01902-1. URL https://doi.org/10.1140/epjp/s13360-021-01902-1.

[2] Filiberto Ares, Sara Murciano, and Pasquale Calabrese. Entanglement asymmetry as a probe of symmetry breaking. *Nature Communications*, 14(1):2036, 2023. DOI: 10.1038/s41467-023-37747-8. URL https://doi.org/10.1038/s41467-023-37747-8.

[3] Filiberto Ares, Sara Murciano, Eric Vernier, and Pasquale Calabrese. Lack of symmetry restoration after a quantum quench: An entanglement asymmetry study. *SciPost Phys.*, 15:089, 2023. DOI: 10.21468/SciPostPhys.15.3.089. URL https://doi.org/10.21468/SciPostPhys.15.3.089.

[4] Hatem Barghathi, C. M. Herdman, and Adrian Del Maestro. Rényi generalization of the accessible entanglement entropy. *Phys. Rev. Lett.*, 121:150501, Oct 2018. DOI: 10.1103/PhysRevLett.121.150501. URL https://doi.org/10.1103/PhysRevLett.121.150501.

[5] Alvise Bastianello, Umberto Borla, and Sergej Moroz. Fragmentation and emergent integrable transport in the weakly tilted ising chain. *Phys. Rev. Lett.*, 128:196601, May 2022. DOI: 10.1103/PhysRevLett.128.196601. URL https://doi.org/10.1103/PhysRevLett.128.196601.

[6] Silas R. Beane, David B. Kaplan, Natalie Klco, and Martin J. Savage. Entanglement suppression and emergent symmetries of strong interactions. *Phys. Rev. Lett.*, 122:102001, Mar 2019. DOI: 10.1103/PhysRevLett.122.102001. URL https://doi.org/10.1103/PhysRevLett.122.102001.

[7] Bruno Bertini, Katja Klobas, Mario Collura, Pasquale Calabrese, and Colin Rylands. Dynamics of charge fluctuations from asymmetric initial states. *Phys. Rev. B*, 109:184312, May 2024. DOI: 10.1103/PhysRevB.109.184312. URL https://doi.org/10.1103/PhysRevB.109.184312.

[8] MJ Bhaseen and AM Tsvelik. Aspects of confinement in low dimensions. *From Fields to Strings: Circumnavigating Theoretical Physics: Ian Kogan Memorial Collection (In 3 Volumes)*, pages 661–683, 2005. DOI: 10.1142/9789812775344_0019. URL https://doi.org/10.1142/9789812775344_0019.

[9] Riccarda Bonsignori, Paola Ruggiero, and Pasquale Calabrese. Symmetry resolved entanglement in free fermionic systems. *Journal of Physics A: Mathematical and Theoretical*, 52(47):475302, 2019. DOI: 10.1088/1751-8121/ab4b77. URL https://dx.doi.org/10.1088/1751-8121/ab4b77.

[10] Umberto Borla, Ruben Verresen, Fabian Grusdt, and Sergej Moroz. Confined phases of one-dimensional spinless fermions coupled to Z_2 gauge theory. *Phys. Rev. Lett.*, 124:120503, Mar 2020. DOI: 10.1103/PhysRevLett.124.120503. URL https://doi.org/10.1103/PhysRevLett.124.120503.

[11] Luca Capizzi and Michele Mazzoni. Entanglement asymmetry in the ordered phase of many-body systems: the Ising field theory. *Journal of High Energy Physics*, 2023(12):144, 2023. DOI: 10.1007/JHEP12(2023)144. URL https://doi.org/10.1007/JHEP12(2023)144.

[12] Luca Capizzi and Vittorio Vitale. A universal formula for the entanglement asymmetry of matrix product states, 2024. URL https://arxiv.org/abs/2310.01962.

[13] Marcela Carena, Ian Low, Carlos E. M. Wagner, and Ming-Lei Xiao. Entanglement Suppression, Enhanced Symmetry and a Standard-Model-like Higgs Boson, 7 2023. URL https://arxiv.org/abs/2307.08112.

[14] Olalla A. Castro-Alvaredo, Máté Lencsés, István M. Szécsényi, and Jacopo Viti. Entanglement oscillations near a quantum critical point. *Phys. Rev. Lett.*, 124:230601, Jun 2020. DOI: 10.1103/PhysRevLett.124.230601. URL https://doi.org/10.1103/PhysRevLett.124.230601.

[15] Alba Cervera-Lierta, José I. Latorre, Juan Rojo, and Luca Rottoli. Maximal Entanglement in High Energy Physics. *SciPost Phys.*, 3:036, 2017. DOI: 10.21468/SciPostPhys.3.5.036. URL https://doi.org/10.21468/SciPostPhys.3.5.036.

[16] Radu Coldea, DA Tennant, EM Wheeler, E Wawrzynska, D Prabhakaran, M Telling, K Habicht, P Smeibidl, and K Kiefer. Quantum criticality in an ising chain: experimental evidence for emergent e8 symmetry. *Science*, 327(5962):177–180, 2010. DOI: 10.1126/science.1180085. URL https://doi.org//10.1126/science.1180085.

[17] David Dasenbrook and Christian Flindt. Dynamical generation and detection of entanglement in neutral leviton pairs. *Phys. Rev. B*, 92:161412, Oct 2015. DOI: 10.1103/PhysRevB.92.161412. URL https://doi.org/10.1103/PhysRevB.92.161412.

[18] Gesualdo Delfino, Giuseppe Mussardo, and P Simonetti. Non-integrable quantum field theories as perturbations of certain integrable

models. *Nuclear Physics B*, 473(3):469–508, 1996. DOI: https://doi.org/10.1016/0550-3213(96)00265-9. URL https://doi.org/10.1016/0550-3213(96)00265-9.

[19] Peter J. Ehlers. Entanglement between valence and sea quarks in hadrons of 1+1 dimensional QCD. *Annals Phys.*, 452:169290, 2023. DOI: 10.1016/j.aop.2023.169290. URL https://doi.org/10.1016/j.aop.2023.169290.

[20] Noa Feldman, Augustine Kshetrimayum, Jens Eisert, and Moshe Goldstein. Entanglement estimation in tensor network states via sampling. *PRX Quantum*, 3:030312, Jul 2022. DOI: 10.1103/PRXQuantum.3.030312. URL https://doi.org/10.1103/PRXQuantum.3.030312.

[21] Florent Ferro, Filiberto Ares, and Pasquale Calabrese. Non-equilibrium entanglement asymmetry for discrete groups: the example of the xy spin chain. *Journal of Statistical Mechanics: Theory and Experiment*, 2024(2):023101, 2024. DOI: 10.1088/1742-5468/ad138f. URL https://dx.doi.org/10.1088/1742-5468/ad138f.

[22] Matthew Fishman, Steven R. White, and E. Miles Stoudenmire. The ITensor Software Library for Tensor Network Calculations. *SciPost Phys. Codebases*, page 4, 2022. DOI: 10.21468/SciPostPhysCodeb.4. URL https://doi.org/10.21468/SciPostPhysCodeb.4.

[23] Matthew Fishman, Steven R. White, and E. Miles Stoudenmire. Codebase release 0.3 for ITensor. *SciPost Phys. Codebases*, pages 4–r0.3, 2022. DOI: 10.21468/SciPostPhysCodeb.4-r0.3. URL https://doi.org/10.21468/SciPostPhysCodeb.4-r0.3.

[24] Zi-Yong Ge, Yu-Ran Zhang, and Franco Nori. Nonmesonic quantum many-body scars in a 1d lattice gauge theory. *Phys. Rev. Lett.*, 132:230403, Jun 2024. DOI: 10.1103/PhysRevLett.132.230403. URL https://doi.org/10.1103/PhysRevLett.132.230403.

[25] Moshe Goldstein and Eran Sela. Symmetry-resolved entanglement in many-body systems. *Phys. Rev. Lett.*, 120:200602, May 2018. DOI: 10.1103/PhysRevLett.120.200602. URL https://doi.org/10.1103/PhysRevLett.120.200602.

[26] Erik J. Gustafson, Andy C. Y. Li, Abid Khan, Joonho Kim, Doga Murat Kurkcuoglu, M. Sohaib Alam, Peter P. Orth, Armin Rahmani, and Thomas Iadecola. Preparing quantum many-body scar states on quantum computers. *Quantum*, 7:1171, Nov 2023. ISSN 2521-327X. DOI: 10.22331/q-2023-11-07-1171. URL https://doi.org/10.22331/q-2023-11-07-1171.

[27] Thomas Iadecola and Michael Schecter. Quantum many-body scar states with emergent kinetic constraints and finite-entanglement revivals. *Phys. Rev. B*, 101:024306, Jan 2020. DOI: 10.1103/PhysRevB.101.024306. URL https://doi.org/10.1103/PhysRevB.101.024306.

[28] Andrew J. A. James, Robert M. Konik, and Neil J. Robinson. Nonthermal states arising from confinement in one and two dimensions. *Phys. Rev. Lett.*, 122:130603, Apr 2019. DOI: 10.1103/PhysRevLett.122.130603. URL https://doi.org/10.1103/PhysRevLett.122.130603.

[29] P. I. Karpov, G.-Y. Zhu, M. P. Heller, and M. Heyl. Spatiotemporal dynamics of particle collisions in quantum spin chains. *Phys. Rev. Res.*, 4:L032001, Jul 2022. DOI: 10.1103/PhysRevResearch.4.L032001. URL https://doi.org/10.1103/PhysRevResearch.4.L032001.

[30] Dmitri E. Kharzeev and Eugene M. Levin. Deep inelastic scattering as a probe of entanglement. *Phys. Rev. D*, 95:114008, Jun 2017. DOI: 10.1103/PhysRevD.95.114008. URL https://doi.org/10.1103/PhysRevD.95.114008.

[31] I. Klich and L. S. Levitov. Scaling of entanglement entropy and superselection rules, 2008. URL https://arxiv.org/abs/0812.0006.

[32] Johannes Knaute, Matan Feuerstein, and Erez Zohar. Entanglement and confinement in lattice gauge theory tensor networks. *Journal of High Energy Physics*, 2024(2):174, 2024. DOI: 10.1007/JHEP02(2024)174. URL https://doi.org/10.1007/JHEP02(2024)174.

[33] Marton Kormos, Mario Collura, Gabor Takács, and Pasquale Calabrese. Real-time confinement following a quantum quench to a non-integrable model. *Nature Physics*, 13(3):246–249, 2017. DOI: 10.1038/nphys3934. URL https://doi.org/10.1038/nphys3934.

[34] Gianluca Lagnese, Federica Maria Surace, Márton Kormos, and Pasquale Calabrese. False vacuum decay in quantum spin chains. *Phys. Rev. B*, 104:L201106, Nov 2021. DOI: 10.1103/PhysRevB.104.L201106. URL https://doi.org/10.1103/PhysRevB.104.L201106.

[35] Gianluca Lagnese, Federica Maria Surace, Sid Morampudi, and Frank Wilczek. Detecting a long lived false vacuum with quantum quenches, 2023. URL https://arxiv.org/abs/2308.08340.

[36] Henry Lamm, Scott Lawrence, and Yukari Yamauchi. Parton physics on a quantum computer. *Phys. Rev. Res.*, 2:013272, Mar 2020. DOI: 10.1103/PhysRevResearch.2.013272. URL https://doi.org/10.1103/PhysRevResearch.2.013272.

[37] Alessio Lerose, Federica M. Surace, Paolo P. Mazza, Gabriele Perfetto, Mario Collura, and Andrea Gambassi. Quasilocalized dynamics from confinement of quantum excitations. *Phys. Rev. B*, 102:041118, Jul 2020. DOI: 10.1103/PhysRevB.102.041118. URL https://doi.org/10.1103/PhysRevB.102.041118.

[38] Fangli Liu, Rex Lundgren, Paraj Titum, Guido Pagano, Jiehang Zhang, Christopher Monroe, and Alexey V. Gorshkov. Confined quasiparticle dynamics in long-range interacting quantum spin chains. *Phys. Rev. Lett.*, 122:150601, Apr 2019. DOI: 10.1103/PhysRevLett.122.150601. URL https://doi.org/10.1103/PhysRevLett.122.150601.

[39] Qiaofeng Liu, Ian Low, and Thomas Mehen. Minimal entanglement and emergent symmetries in low-energy qcd. *Phys. Rev. C*, 107:025204, Feb 2023. DOI: 10.1103/PhysRevC.107.025204. URL https://doi.org/10.1103/PhysRevC.107.025204.

[40] Paolo Pietro Mazza, Gabriele Perfetto, Alessio Lerose, Mario Collura, and Andrea Gambassi. Suppression of transport in nondisordered quantum spin chains due to confined excitations. *Phys. Rev. B*, 99:180302, May 2019. DOI: 10.1103/PhysRevB.99.180302. URL https://doi.org/10.1103/PhysRevB.99.180302.

[41] Barry M. McCoy and Tai Tsun Wu. Two-dimensional ising field theory in a magnetic field: Breakup of the cut in the two-point function. *Phys. Rev. D*, 18:1259–1267, Aug 1978. DOI: 10.1103/PhysRevD.18.1259. URL https://link.aps.org/doi/10.1103/PhysRevD.18.1259.

[42] Ashley Milsted, Junyu Liu, John Preskill, and Guifre Vidal. Collisions of false-vacuum bubble walls in a quantum spin chain. *PRX Quantum*, 3:020316, Apr 2022. DOI: 10.1103/PRXQuantum.3.020316. URL https://doi.org/10.1103/PRXQuantum.3.020316.

[43] Sara Murciano, Giuseppe Di Giulio, and Pasquale Calabrese. Entanglement and symmetry resolution in two dimensional free quantum field theories. *Journal of High Energy Physics*, 2020(8):73, 2020. DOI: 10.1007/JHEP08(2020)073. URL https://doi.org/10.1007/JHEP08(2020)073.

[44] Sara Murciano, Pasquale Calabrese, and Lorenzo Piroli. Symmetry-resolved page curves. *Phys. Rev. D*, 106:046015, Aug 2022. DOI: 10.1103/PhysRevD.106.046015. URL https://doi.org/10.1103/PhysRevD.106.046015.

[45] Sara Murciano, Filiberto Ares, Israel Klich, and Pasquale Calabrese. Entanglement asymmetry and quantum mpemba effect in the xy spin chain. *Journal of Statistical Mechanics: Theory and Experiment*, (1):013103, Jan 2024. DOI: 10.1088/1742-5468/ad17b4. URL https://dx.doi.org/10.1088/1742-5468/ad17b4.

[46] Antoine Neven, Jose Carrasco, Vittorio Vitale, Christian Kokail, Andreas Elben, Marcello Dalmonte, Pasquale Calabrese, Peter Zoller, Benoit Vermersch, Richard Kueng, and Barbara Kraus. Symmetry-resolved entanglement detection using partial transpose moments. *npj Quantum Information*, 7(1):152, 2021. DOI: 10.1038/s41534-021-00487-y. URL https://doi.org/10.1038/s41534-021-00487-y.

[47] Michael A. Nielsen and Isaac L. Chuang. *Quantum Computation and Quantum Information: 10th Anniversary Edition*. Cambridge University Press, 2011. ISBN 9781107002173. DOI: https://doi.org/10.1017/CBO9780511976667.

[48] Maike Ostmann, Matteo Marcuzzi, Juan P. Garrahan, and Igor Lesanovsky. Localization in spin chains with facilitation constraints and disordered interactions. *Phys. Rev. A*, 99:060101, Jun 2019. DOI: 10.1103/PhysRevA.99.060101. URL https://doi.org/10.1103/PhysRevA.99.060101.

[49] O. Pomponio, M. A. Werner, G. Zarand, and G. Takacs. Bloch oscillations and the lack of the decay of the false vacuum in a one-dimensional quantum spin chain. *SciPost Phys.*, 12:061, 2022. DOI: 10.21468/SciPostPhys.12.2.061. URL https://doi.org/10.21468/SciPostPhys.12.2.061.

[50] Nishan Ranabhat, Alessandro Santini, Emanuele Tirrito, and Mario Collura. Dynamical deconfinement transition driven by density of excitations, 2023. URL https://arxiv.org/abs/2310.02320.

[51] Aniket Rath, Vittorio Vitale, Sara Murciano, Matteo Votto, Jérôme Dubail, Richard Kueng, Cyril Branciard, Pasquale Calabrese, and Benoit Vermersch. Entanglement barrier and its symmetry resolution: Theory and experimental observation. *PRX Quantum*, 4:010318, Feb 2023. DOI: 10.1103/PRXQuantum.4.010318. URL https://doi.org/10.1103/PRXQuantum.4.010318.

[52] Neil J. Robinson, Andrew J. A. James, and Robert M. Konik. Signatures of rare states and thermalization in a theory with confinement. *Phys. Rev. B*, 99:195108, May 2019. DOI: 10.1103/PhysRevB.99.195108. URL https://doi.org/10.1103/PhysRevB.99.195108.

[53] S. B. Rutkevich. Decay of the metastable phase in $d = 1$ and $d = 2$ ising models. *Phys. Rev. B*, 60:14525–14528, Dec 1999. DOI:

10.1103/PhysRevB.60.14525. URL https://doi.org/10.1103/PhysRevB.60.14525.

[54] SB Rutkevich. Energy spectrum of bound-spinons in the quantum ising spin-chain ferromagnet. *Journal of Statistical Physics*, 131(5):917–939, 2008. DOI: 10.1007/s10955-008-9495-1. URL https://doi.org/10.1007/s10955-008-9495-1.

[55] Stefano Scopa, Pasquale Calabrese, and Alvise Bastianello. Entanglement dynamics in confining spin chains. *Phys. Rev. B*, 105:125413, Mar 2022. DOI: 10.1103/PhysRevB.105.125413. URL https://doi.org/10.1103/PhysRevB.105.125413.

[56] Alejandro Sopena, Max Hunter Gordon, Germán Sierra, and Esperanza López. Simulating quench dynamics on a digital quantum computer with data-driven error mitigation. *Quantum Science and Technology*, 6:045003, July 2021. DOI: 10.1088/2058-9565/ac0e7a. URL https://dx.doi.org/10.1088/2058-9565/ac0e7a.

[57] Roberto Verdel, Fangli Liu, Seth Whitsitt, Alexey V. Gorshkov, and Markus Heyl. Real-time dynamics of string breaking in quantum spin chains. *Phys. Rev. B*, 102:014308, Jul 2020. DOI: 10.1103/PhysRevB.102.014308. URL https://doi.org/10.1103/PhysRevB.102.014308.

[58] Roberto Verdel, Guo-Yi Zhu, and Markus Heyl. Dynamical localization transition of string breaking in quantum spin chains. *Phys. Rev. Lett.*, 131:230402, Dec 2023. DOI: 10.1103/PhysRevLett.131.230402. URL https://doi.org/10.1103/PhysRevLett.131.230402.

[59] F. Verstraete, J. J. García-Ripoll, and J. I. Cirac. Matrix product density operators: Simulation of finite-temperature and dissipative systems. *Phys. Rev. Lett.*, 93:207204, Nov 2004. DOI: 10.1103/PhysRevLett.93.207204. URL https://doi.org/10.1103/PhysRevLett.93.207204.

[60] Guifré Vidal. Efficient simulation of one-dimensional quantum many-body systems. *Phys. Rev. Lett.*, 93:040502, Jul 2004. DOI: 10.1103/PhysRevLett.93.040502. URL https://doi.org/10.1103/PhysRevLett.93.040502.

[61] Vittorio Vitale, Andreas Elben, Richard Kueng, Antoine Neven, Jose Carrasco, Barbara Kraus, Peter Zoller, Pasquale Calabrese, Benoit Vermersch, and Marcello Dalmonte. Symmetry-resolved dynamical purification in synthetic quantum matter. *SciPost Phys.*, 12:106, 2022. DOI: 10.21468/SciPostPhys.12.3.106. URL https://doi.org/10.21468/SciPostPhys.12.3.106.

[62] Joseph Vovrosh and Johannes Knolle. Confinement and entanglement dynamics on a digital quantum computer. *Sci. Rep.*, 11(1):11577, 2021. DOI: 10.1038/s41598-021-90849-5.

[63] Joseph Vovrosh, Rick Mukherjee, Alvise Bastianello, and Johannes Knolle. Dynamical hadron formation in long-range interacting quantum spin chains. *PRX Quantum*, 3:040309, Oct 2022. DOI: 10.1103/PRXQuantum.3.040309. URL https://doi.org/10.1103/PRXQuantum.3.040309.

[64] Steven R. White and Adrian E. Feiguin. Real-time evolution using the density matrix renormalization group. *Phys. Rev. Lett.*, 93:076401, Aug 2004. DOI: 10.1103/PhysRevLett.93.076401. URL https://doi.org/10.1103/PhysRevLett.93.076401.

[65] Kenneth G. Wilson. Confinement of quarks. *Phys. Rev. D*, 10:2445–2459, Oct 1974. DOI: 10.1103/PhysRevD.10.2445. URL https://doi.org/10.1103/PhysRevD.10.2445.

[66] Zhao Zhang, Kirill Amelin, Xiao Wang, Haiyuan Zou, Jiahao Yang, Urmas Nagel, Toomas Rõom, Tusharkanti Dey, Agustinus Agung Nugroho, Thomas Lorenz, Jianda Wu, and Zhe Wang. Observation of E_8 particles in an ising chain antiferromagnet. *Phys. Rev. B*, 101:220411, Jun 2020. DOI: 10.1103/PhysRevB.101.220411. URL https://doi.org/10.1103/PhysRevB.101.220411.

[67] Haiyuan Zou, Yi Cui, Xiao Wang, Z. Zhang, J. Yang, G. Xu, A. Okutani, M. Hagiwara, M. Matsuda, G. Wang, Giuseppe Mussardo, K. Hódsági, M. Kormos, Zhangzhen He, S. Kimura, Rong Yu, Weiqiang Yu, Jie Ma, and Jianda Wu. E_8 spectra of quasi-one-dimensional antiferromagnet baco$_2$v$_2$o$_8$ under transverse field. *Phys. Rev. Lett.*, 127:077201, Aug 2021. DOI: 10.1103/PhysRevLett.127.077201. URL https://doi.org/10.1103/PhysRevLett.127.077201.

A Benchmarking exact diagonalization, two-kink dynamics and tensor network simulations

In this appendix, we present numerical data benchmarking. (1) We study the time evolution dynamics of the spin, initial domain wall, and Rényi entropy for both the exact diagonalization and the two-kink Hamiltonian dynamics, both at the special point $J = -g$ (where they should match) and $J \neq -g$ (where they generally differ). (2) We compare the time evolution dynamics for the initial domain wall and Rényi entropy for tensor network simulation
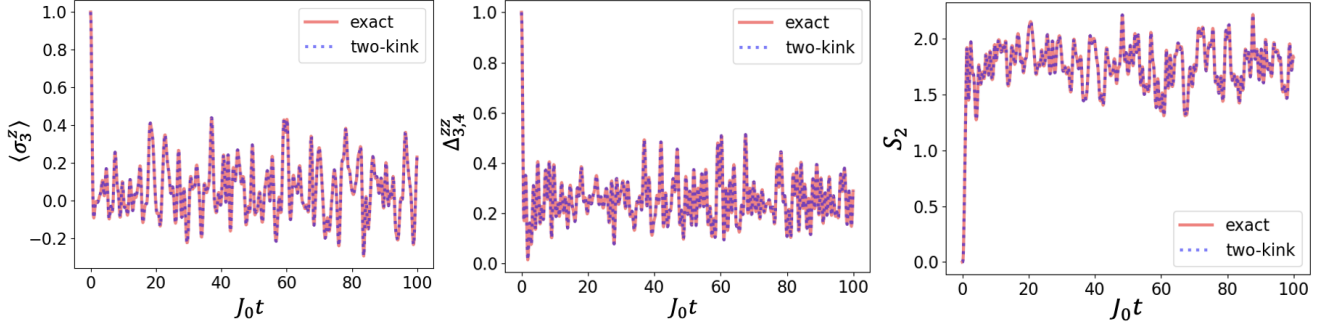
and two-kink dynamics for larger system size.

Figure 7: From left to right: The spin expectation value $\langle \sigma_3^z \rangle$, the domain wall expectation value $\Delta_{3,4}^{zz}$ and the half chain Rényi entropy S_2 at parameter values $g = 0.7 = -J, h = 0.1$ for both exact and two-kink dynamics. At this special point where $g = -J$, the time evolution dynamics for the exact diagonalization can be described exactly by two-kink subspace dynamics.
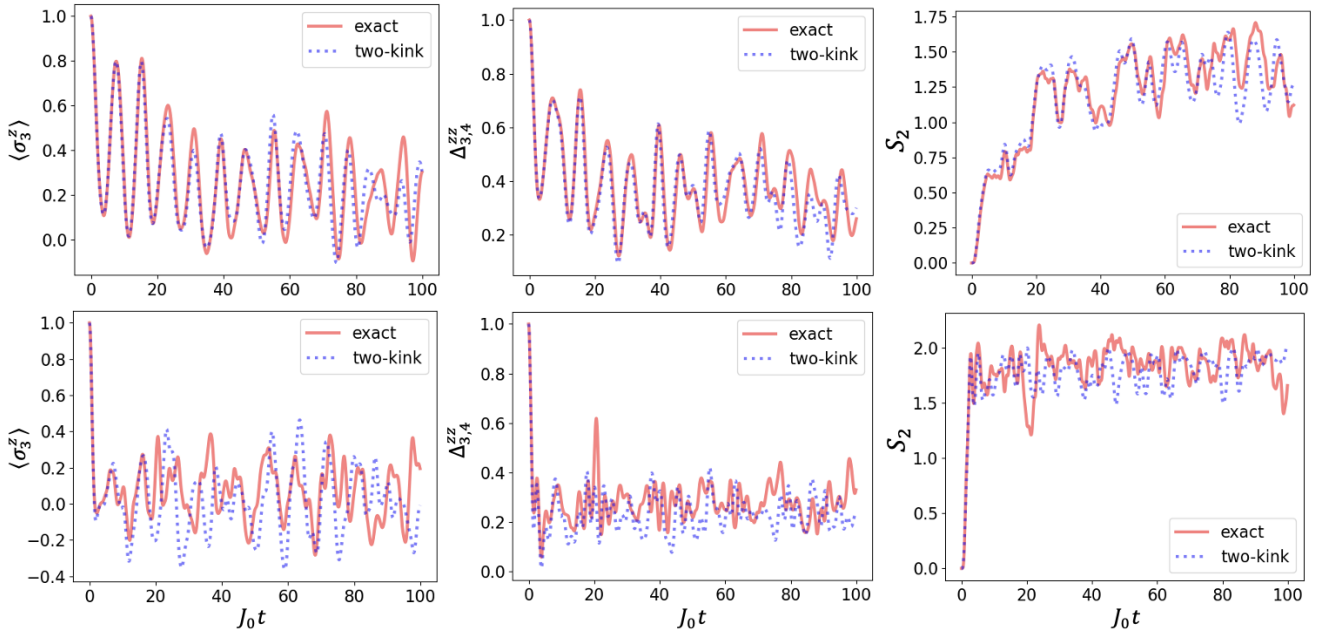

Figure 8: From left to right: The spin expectation value $\langle \sigma_3^z \rangle$, the domain wall expectation value $\Delta_{3,4}^{zz}$ and the half chain Rényi entropy S_2. From top to bottom: The set of physical quantities at the top panel was simulated at $g = 0.3, h = 0.4$ and $J = -0.05$ while the bottom panel was at $g = 0.6, h = 0.1, J = -0.1$. Note that the top panel corresponds to a more confined dynamics, where the deviation of the time evolution and exact diagonalization occurs only at late time, while for parameter with less confinement (smaller h), the deviation is significant even at early times.

For the first benchmarking between exact diagonalization and two-kink dynamics (to establish the reliability of two-kink dynamics in kink-conserving cases), we initialize the quantum state of a $L = 10$ quantum Ising spin chain to $|\psi_0\rangle = |\uparrow\uparrow\uparrow\uparrow\downarrow\downarrow\uparrow\uparrow\uparrow\uparrow\rangle$, and time evolve the state using (a) exact diagonalization of the Hamiltonian Eq. 1 in the main text and (b) two-kink Hamiltonian Eq. 4 in the main text. For Fig. 7 and 8, the spin expectation values $\langle \sigma_i^z(t) \rangle$ are tracked at the underlined spin $|\uparrow\uparrow\uparrow \underline{\uparrow} \downarrow\downarrow\uparrow\uparrow\uparrow\uparrow\rangle$ in the initial state $|\psi_0\rangle$, and the domain wall expectation values $\Delta_{i,i+1}^{zz}(t)$ are tracked at $|\uparrow\uparrow\uparrow \underline{\uparrow\downarrow} \downarrow\uparrow\uparrow\uparrow\uparrow\rangle$, and the Rényi entropy is cut at half chain bipartition respectively.

In Fig. 7, we see that the time evolution of the various different physical quantities of interest match between exact diagonalization and two-kink subspace evolution. As demanded by the symmetry of the Hamiltonian when $g = -J$, the domain wall number at this special line is exactly conserved.

We then turn to the string breaking (more generic) cases, where kink number is not conserved. In Fig. 8, we observe that while we generally expect the dynamics of the exact Hamiltonian to differ from that from the two-kink subspace projection at $g \neq -J$, the macroscopic expectation values for spin $\langle \sigma_i^z \rangle$ and domain wall $\Delta_{i,i+1}^z$ overlaps significantly for early times and only deviate at later time for strong confining field h. In contrast, with weak confining field h the dynamics deviates significantly at early times. This establishes the general physics and intuition that with strong confinement h, two-kink approximation is reasonable for quantum quench problem with initial state $| \uparrow \ldots \uparrow \downarrow \ldots \downarrow \uparrow \ldots \uparrow \rangle$.
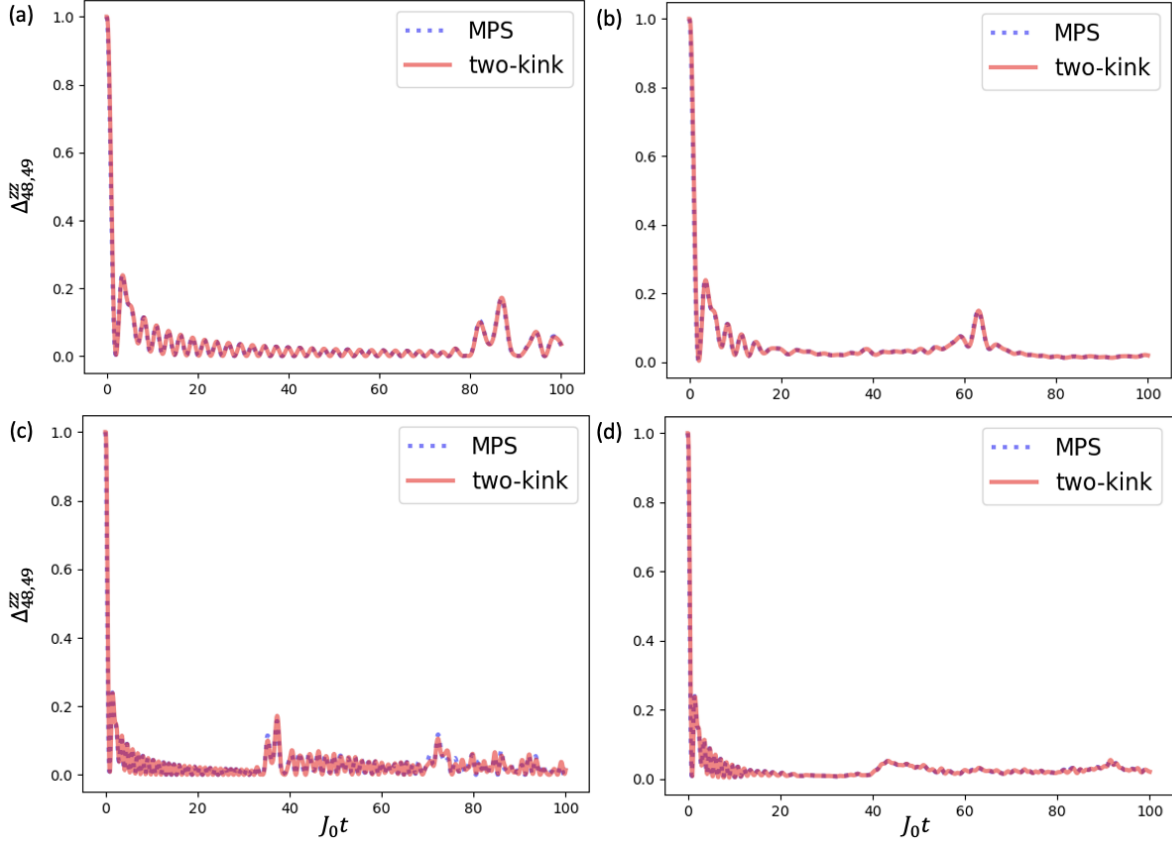

Figure 9: The set of parameter values used for the time evolution of the domain wall $\Delta_{48,49}^{zz}$ at position 48 and 49 following a quantum quench are (a) $g = 0.3, J = -0.3, h = 0$, (b) $g = 0.3, J = -0.3, h = 0.05$, (c) $g = 0.7, J = -0.7, h = 0.0$, (d) $g = 0.7, J = -0.7, h = 0.05$.

After verifying the validity of the two-kink dynamics for kink-conserving dynamics, we then turn to the benchmarking of the tensor network simulations with the two-kink dynamics. In the main article, we provided the benchmarking of MPS with two-kink dynamics for the time evolution of the Rényi entropy S_2 for $g = -J = 0.7$ in Fig. 1 in the main text. Here, we provide additional numerical simulations of the domain wall profile located at the initial domain wall positions at 48th and 49th sites for a spin chain of length $L = 100$ and initial state with 4 middle flipped spin $| \uparrow_1 \ldots \uparrow_{48} \downarrow_{49} \downarrow_{50} \downarrow_{51} \downarrow_{52} \uparrow_{53} \ldots \uparrow_{100} \rangle$, as shown in Fig. 9. This provides an additional check (besides the Rényi entropy dynamics) that the MPS time evolution from TEBD is approximated well by two-kink time evolution.

B Construction of the reduced density matrix in the Two-Kink Subspace

In this section, we outline the overall approach we used to construct the reduced density matrix in the two-kink subspace in order to calculate the 2nd order Rényi entropy for dynamics within the two-kink subspace. We represent all possible two-kink states in a spin chain of length L, $| \uparrow_1 \ldots \uparrow_{j_L-1} \downarrow_{j_L} \ldots \downarrow_{j_R} \uparrow_{j_R+1} \ldots \uparrow_L \rangle$, with the two number

representation $|j_L, j_R\rangle$, where j_L is the position of the left domain wall and j_R is the position of the right domain wall. In the two-kink Hilbert space, for sites $i = 1, \ldots, L$, the two numbers can take the following values $1 < j_L \leq j_R < L$.

With this two-number representation, a quantum spin chain of size L will have a two-kink subspace of dimension $(L-1)(L-2)/2$. To proceed with the Rényi entropy calculation, given a bipartition bond l_B separating the spin chain into left-right bipartition with sites $1, \ldots, l_B$ to the left side of the chain and sites $l_B + 1, \ldots, L$ to the right, we will proceed to perform bipartition in the two-kink states

$$
\begin{aligned}
|\psi\rangle &= \sum_{1 < j_L \leq j_R \leq l_B < L} \alpha_{j_L, j_R} |\text{one/two-kink}\rangle_L |\text{no-kink}\rangle_R + \sum_{1 < j_L \leq l_B < j_R < L} \alpha_{j_L, j_R} |\text{one-kink}\rangle_L |\text{one-kink}\rangle_R \\
&+ \sum_{1 \leq l_B < j_L \leq j_R < L} \alpha_{j_L, j_R} |\text{no-kink}\rangle_L |\text{one/two-kink}\rangle_R,
\end{aligned} \tag{18}
$$

where we decompose the sum into three types of terms classified by the location of the bipartition cut relative to the domain wall positions. Here, the states with label $|\text{one-kink}\rangle_L |\text{no-kink}\rangle_R$ and $|\text{no-kink}\rangle |\text{one-kink}\rangle_R$ are cases where the bipartition cut l_B coincides with one of the left/right domain walls.

Constructing the full pure state density matrix $|\psi\rangle\langle\psi|$ and taking the partial trace over the right partition, we have

$$
\begin{aligned}
\rho_L &= \text{Tr}_R(|\psi\rangle\langle\psi|) = \sum_{1 < j_L \leq j_R \leq l_B} \sum_{1 < j'_L \leq j'_R \leq l_B} \alpha_{j_L, j_R} \alpha^*_{j'_L, j'_R} |\text{one/two-kink}\rangle\langle\text{one/two-kink}| \\
&+ \sum_{1 < j_L \leq l_B} \sum_{1 < j'_L \leq l_B} \left(\sum_{l_B < j_R < L} \alpha_{j_L, j_R} \alpha^*_{j'_L, j_R} \right) |\text{one-kink}\rangle\langle\text{one-kink}| \\
&+ \left(\sum_{l_B < j_L \leq j_R < L} \alpha_{j_L, j_R} \alpha^*_{j_L, j_R} \right) |\text{no-kink}\rangle\langle\text{no-kink}| \\
&+ \sum_{1 < j_L \leq l_B} \left(\sum_{l_B < j_R < L} \alpha_{j_L, j_R} \alpha^*_{j'_L = l_B + 1, j_R} \right) |\text{one-kink}\rangle\langle\text{no-kink}| \\
&+ \sum_{1 < j'_L \leq l_B} \left(\sum_{l_B < j_R < L} \alpha^*_{j'_L, j_R} \alpha_{j_L = l_B + 1, j_R} \right) |\text{no-kink}\rangle\langle\text{one-kink}|
\end{aligned} \tag{19}
$$

We shall elaborate on each term below.

The first term

The first term in Eq. (19) is obtained from the multiplying the first terms of Eq. (18) in both $|\psi\rangle$ and $\langle\psi|$, followed by partial right trace over all spin-up state $|\text{no-kink}\rangle_R$. Hence, the coefficients in the first term in Eq. (19) can be understood to be constructed without performing any sum from partial tracing.

The second term

The second term in Eq. (19) is obtained by multiplying the second terms of Eq. (18) in both $|\psi\rangle$ and $\langle\psi|$, followed by partial right trace over $|\text{one-kink}\rangle_R$. In this case, the coefficients in the second term in Eq. (19) is constructed from summing over $l_B < j_R = j'_R < L$ where the right partition states $|\text{one-kink}\rangle$ and $\langle\text{one-kink}|$ must agree in the partial trace process.

We also note here that terms labelled as 'the second term' is actually a subset of 'the first term' and not a new set of distinct terms (which we label separately only because they had different origin), so the coefficients here should add to the coefficients of the first term when the states are the same.

The third term

The third term in Eq. (19) is actually a single state, and its coefficient is constructed from a sum over the modulo square $|\alpha_{j_L, j_R}|^2$ for $l_B < j_L \leq j_R < L$. Here j_L and j_R both lie on the right partition basis states, for which the

indices must match (hence mod square) when one performs the partial trace.

The fourth and fifth terms

The fourth and the fifth term in Eq. (19) are the complex conjugate of each other, so it suffices to explain one of them. The fourth term comes from the cross multiplication of the second term $|$one-kink$\rangle|$one-kink$\rangle$ and the third term of type $\langle$no-kink$|\langle$one-kink$|$ in Eq. (18).

Note that the third term of the form $\langle$no-kink$|\langle$two-kink$|$ cannot contribute since the right partition partial cannot match those from $|$one-kink$\rangle|$one-kink$\rangle$. This explains the setting of $j'_L = l_B + 1$ in the coefficient of the fourth term (likewise the corresponding term in the fifth term). We also understand that there is a single sum matching the indices $j_R = j'_R$ over the range $l_B < j_R < L$ when one construct the coefficients of the fourth and the fifth term.

Matrix representation of the reduced density matrix

Collecting these terms, it helps to visualize these various terms on a matrix representation. We label row sectors according to $|$two-kink$\rangle$, $|$one-kink$\rangle$ and $|$no-kink$\rangle$ and likewise for the column sectors. The matrix representation is as below.

$$
\rho_L = \begin{pmatrix}
\begin{array}{c} \text{First term} \\ |\text{two-kink}\rangle\langle\text{two-kink}| \end{array} & \begin{array}{c} \text{First term} \\ |\text{two-kink}\rangle\langle\text{one-kink}| \end{array} & 0 \\
\hline
\begin{array}{c} \text{First term} \\ |\text{one-kink}\rangle\langle\text{two-kink}| \end{array} & \begin{array}{c} \text{First + Second term} \\ |\text{one-kink}\rangle\langle\text{one-kink}| \end{array} & \begin{array}{c} \text{Fourth term} \\ |\text{one-kink}\rangle\langle\text{no-kink}| \end{array} \\
\hline
0 & \begin{array}{c} \text{Fifth term} \\ |\text{no-kink}\rangle\langle\text{one-kink}| \end{array} & \begin{array}{c} \text{Third term} \\ |\text{no-kink}\rangle\langle\text{no-kink}| \end{array}
\end{pmatrix}
$$

Here, the third row is a single row and the third column is a single column. The reduced density matrix can then be used to calculate the Rényi entropy for the two-kink dynamics.

C   Rényi Entropy Evolution and Collisions: Early time and Entropy bound violation with large system size

In this appendix, we cover two points. (1) We outline several qualitative features of the Rényi entropy evolution that highlight several interesting features that are not discussed in the main article. (2) In addition, we show that the entropy bound violation with confining field is independent of the finite system size effect. We will mainly concern ourselves with the kink-preserving dynamics in this appendix.

For generic model parameters, as the initial product state domain wall starts evolving, entanglement immediately appears, dominated by the dynamics of kink-anti kink pair creation and motion. In contrast, for kink-number preserving dynamics, the half-chain entanglement can only begin emerging when the kinks collide. To see this, we compute the Rényi entropy of half of the chain. In Fig. 10, we show how a rapid increase in the half-chain Rényi entropy S_2 for small domain wall and large domain wall separation is associated to the time of the domain wall spreading and collision. Here, a small initial domain wall separation ($l = 4$) has a collision around $t \approx 1$ while that of the large separation $l = 24$ has collision around $t \approx 5$.

We provide additional details for the Rényi entropy dips found in Fig. 5 in the main text. Here, the dip around $t \approx 85$ is directly associated with kink collision after bouncing off the open boundary chain. We provide the associated domain wall/kink heatmap in Fig. 11.

We now turn to demonstrate that the violation of the $S_2 = 2$ bound is independent of the system size, along with other qualitative features of the entropy evolution. In Fig. 12, we vary various parameters within the kink-conserving dynamics: (1) the kinetic energy $(g - J)$, (2) the confining potential field h, and (3) the system size L.

In Fig. 12, we see the S_2 entropy bound is violated upon the second collision of the kinks. The first collision happens at early time and is discussed in detail earlier in this appendix. Here, we verify that the total kink density near the ends of the chain is negligible when the second collision occurs upon the acceleration of the kink dynamics back to the middle of the chain owing to the confining potential.
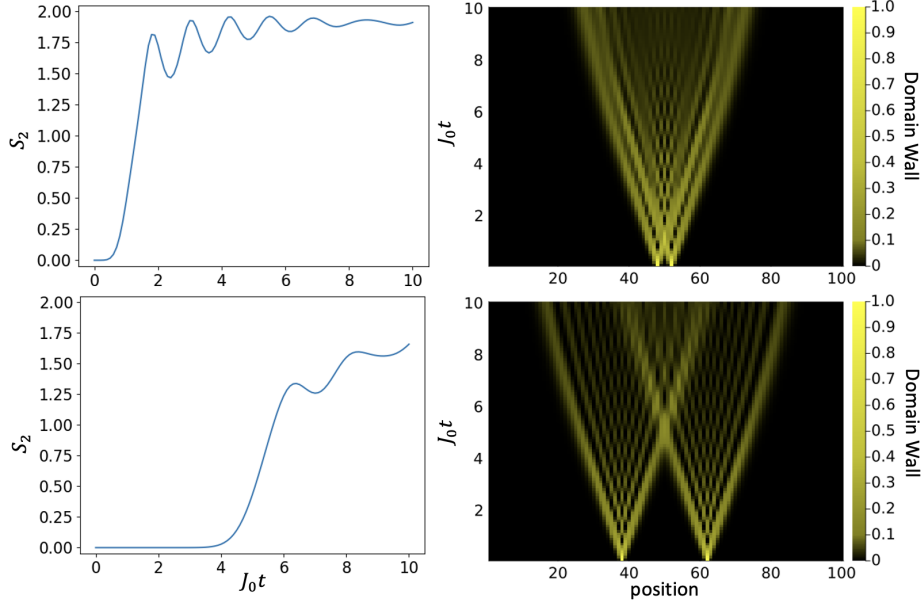
Figure 10: The half-chain Rényi entropy S_2 (left) and the domain wall profile across link positions (right) for the parameter value set $g = -J = 0.7, h = 0.1$. Here the top diagrams are results from initial state with domain wall separation $l = 4$ (4 down spins in the middle) while the bottom diagrams are results with initial domain wall separation $l = 24$. The increase in S_2 in the early time roughly coincides with the time scale of collision for kink-conserving dynamics. The spin chain is of length $L = 100$.

Another feature of the kink-conserving dynamics is the dip in the Rényi entropy before the periodic collisions of the kinks after expanding to maximal extent set by the strength of the confining potential. This can be observed in the half-chain Rényi entropy, as well as in the Rényi entropy heatmap diagram, where the color code shows a lower Rényi entropy dip right before the periodic collisions of the kinks.

D MPS Implementation and Computational Complexity

Many $1D$ systems can be analyzed efficiently using matrix product states (MPS). Previous work has explored entanglement asymmetry in the context of exact diagonalization [2], where large system sizes can only be explored for non-interacting models, and iTEBD time evolution for interacting models with integrability [7]. Another recent work [12] has explored entanglement asymmetry in matrix product states in the context of the ground state of a symmetric Hamiltonian undergoing spontaneous symmetry breaking. Here we implement the computation of the ΔS_2 entanglement asymmetry given an MPS for generic models that includes non-integrability, an interacting Hamiltonian, and a more general setting that includes non-local entanglement asymmetry.

We will now outline the general algorithm for the straightforward computation of the bipartite entanglement asymmetry for MPS.

1. Perform the time evolution of the MPS from $|\psi(t - \Delta t)\rangle$ to $|\psi(t)\rangle$ with the choice of tMPS, tDMRG or TEBD.

2. Choose the orthogonality center of the MPS across which the bipartite 2nd Rényi entropy $S_2(\rho_A)$ is calculated (mixed canonical MPS).

3. Contract the indices efficiently (with increasing bond dimensions) from one end of the MPS to the orthogonal center to construct the reduced density matrix ρ_A (Fig. 13(a)).

4. With ρ_A, split the numerical integration of Eq. 15 in the main text into $k + 1$ steps. For each discrete λ perform the MPO application onto the ρ_A [Fig. 13(b) or (c)]. Perform the full trace after evaluating $e^{i\lambda Q} \rho_A e^{-i\lambda Q} \rho_A$. The MPO application and tracing is done $k + 1$ times to evaluate $S_2(\rho_{A,Q})$ and subsequently ΔS_2.
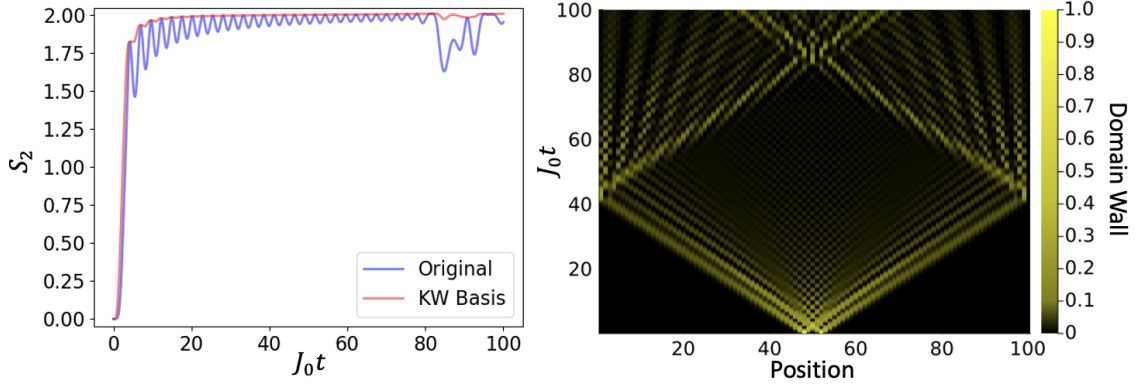
Figure 11: The half-chain Rényi entropy S_2 (left) and domain wall heat (right) for $g = -J = 0.3$, $h = 0$, $L = 100$, and initial domain wall separation size $l = 4$. The dip around $t \approx 85$ corresponds to kink collisions. The color scale has been magnified near $\Delta_{i,i+1}^{zz} = 0$ as the kink density becomes diluted upon spreading.

In this work, we calculate two different types of entanglement asymmetry: onsite entanglement asymmetry (such as the magnetization entanglement asymmetry previous considered in [2] with $Q_A = \sum_{i=2}^{l} \sigma_i^z$) and link-type entanglement asymmetry (in our case, the kink entanglement asymmetry with $Q_A = \sum_{i=1}^{l-1} \sigma_i^z \sigma_{i+1}^z$, shown in Fig. 13(c)).

We will comment on the computational complexity of our algorithm above, and possible speed up that could possibly be implemented in a future work. In iTensor, working with density matrices is actually sub-optimal since it creates MPO with bond dimension D^2, which we illustrate in Fig. 14. Depending on the details of how iTensor package handles the contraction of two (different) reduced density matrices, this computation can either scale as $\mathcal{O}(Ld^3D^8)$ in the worst case or $\mathcal{O}(Ld^3D^6)$ in the most optimal case. Dealing with reduced density matrices directly is more straightforward in code development with existing methods in iTensor, but severely limits the simulability of Rényi entropy evolution to later times when bond dimension is large everywhere on the spin chain. This is the case for string breaking (kink number violating, generic case) situation when $g \neq -J$, as shown in Fig. 6 in the main text when we attempt to calculate Rényi asymmetry directly with density matrix contractions and issue with computational cost only allows time evolution for early times ($t = 10$).

Instead, an optimal approach is shown in Fig. 15. The algorithm represented pictorially in Fig. 15 will necessitate contractions without constructing reduced density matrices directly. In this approach, we contract tensors individually and avoid the dealing with the full D^2 bond dimensions of each ρ_A MPO link. The algorithm in this case will dramatically improves the complexity to $\mathcal{O}(LdD^3)$, but it comes with a more complicated code development. We will leave the development of a more efficient entanglement asymmetry computation as a future research avenue.

E Kramers-Wannier Unitary Transformation and the XY Model

Given the problem that the kink entanglement asymmetry at the interface cannot be tracked in our current basis, we perform a site-to-link transformation to map link variables (such as the domain wall operator $\sigma_i^z \sigma_{i+1}^z$) to site variable. This has traditionally been associated to the Kramers-Wannier duality on a 2D Ising Model. In the context of the (1+1)D Transverse Field Ising Model, one cannot construct a unitary that represents the Kramers-Wannier duality since it maps the ferromagnetic phase of the Transverse Field Ising model ($g < 1$) with ground state degeneracy and spin-flip symmetry breaking to the paramagnetic phase of the Transverse Field Ising Model ($g > 1$) with non-degenerate ground state possessing spin-flip symmetry. Hence, we wish to clarify from the onset that our unitary defined below is a Kramers-Wannier unitary transformation that is only well-defined on an open chain and serves to perform a basis transformation.

We define a Kramers-Wannier unitary U_{KW} that is distinct from the Kramers-Wannier duality in the sense that: (1) it is defined on open boundary condition, (2) it maps all links to sites except the first site, which also maps to the first site in the 'dual' lattice, and (3) the unitary is not self-dual, i.e., $U_{KW}^2 \neq I$. In this way the dimension of the Hilbert space is preserved, since an open chain with N sites only has $N - 1$ links. The unitary is defined and
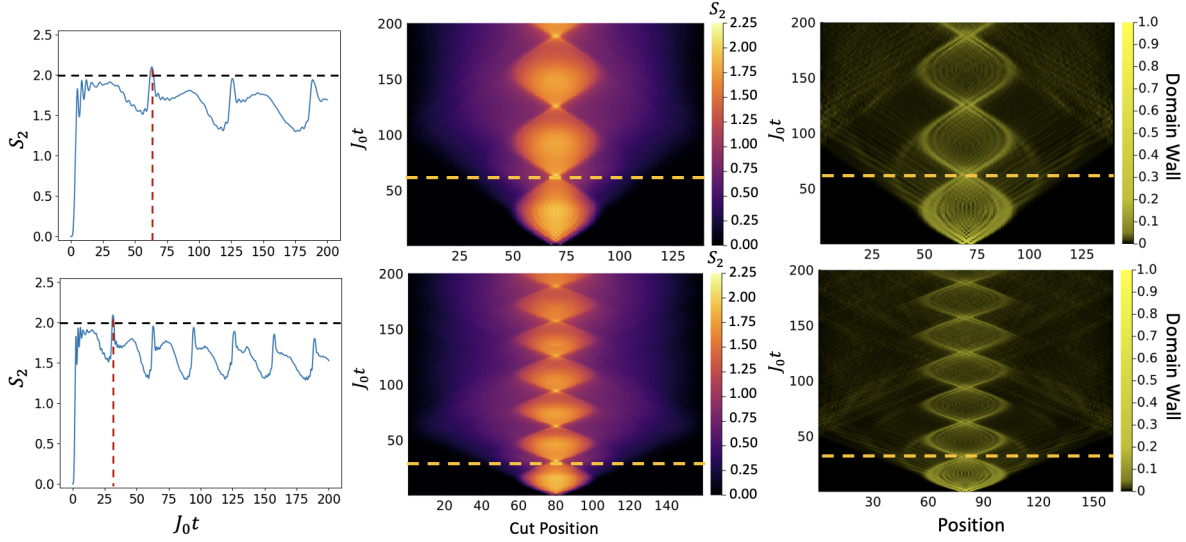
Figure 12: The half-chain Rényi entropy S_2 (left), the Rényi entropy map with different bipartite cut position (middle), and the domain wall profile across link positions (right) for $g = -J = 0.25, h = 0.05, L = 140$ (top) and $g = -J = 0.5, h = 0.1, L = 160$ (bottom).

represented in the quantum circuit language as a series of CNOT gates, as shown in Fig. 16.

Here, we have defined $|0\rangle \equiv |\uparrow\rangle \equiv |s = +1\rangle$, $|1\rangle \equiv |\downarrow\rangle \equiv |s = -1\rangle$, and one can verify that the action of the CNOT gate on the target qubit/spin matches the value of the product of spin $t_j = s_{j-1}s_j$. In this dual lattice picture, we can perform the unitary transformation on the Hamiltonian $H' = U_{KW} H U_{KW}^\dagger$ to get, in this dual picture,

$$H' = -\left[J_0 \sum_{i=2}^{L} \sigma_i^z + g \sum_{i=2}^{L-1} \sigma_i^x \sigma_{i+1}^x + h \sum_{i=1}^{L} \left(\prod_{j=1}^{i} \sigma_j^z \right) - J \sum_{i=2}^{L-1} \sigma_i^y \sigma_{i+1}^y \right], \tag{20}$$

where the Kramers-Wannier unitary U_{KW} maps $\sigma_i^z \to \prod_{j=1}^{i} \sigma_j^z$, $\sigma_i^x \to \sigma_i^x \sigma_{i+1}^x$, and the coefficients above identify the origin of the terms of the original Hamiltonian in Eq. 1 in the main text. While the form of the Kramers-Wannier mapping for σ_i^z and σ_i^x has been given in [48], to our knowledge the explicit form of the unitary has not been given in earlier works. In this dual picture, the symmetry operator is transformed as $\prod_{i=1}^{l-1} e^{\pm i\lambda \sigma_i^z \sigma_{i+1}^z} \to \prod_{i=2}^{l} e^{\pm i\lambda \sigma_i^z}$, the total magnetization of the left half of the spin chain except the magnetization on site 1.

Interestingly, while the original Hamiltonian had 4 sectors associated with local boundary spins σ_1^z and σ_L^z, our transformed Hamiltonian now commutes with σ_1^z as well as with the parity operator $\prod_{i=1}^{L} \sigma_i^z$ which is non-local. We also note that the original Hamiltonian preserves the parity of the kink number, even when $g \neq -J$. This form also makes explicit the conservation of kink parity, where kink is now represented by the number of down spins.

When $h = 0$ in the Hamiltonian Eq. (20), this Hamiltonian is the XY model. This can readily be cast into the free fermion picture using the Jordan Wigner Transformation, with the resulting Hamiltonian (ignoring constant terms)

$$H = -\left[2J_0 \sum_{j=2}^{L} c_j^\dagger c_j + (g+J) \sum_{j=2}^{L-1} (c_j^\dagger c_{j+1}^\dagger + c_{j+1} c_j) + (g-J) \sum_{j=2}^{L-1} (c_j^\dagger c_{j+1} + c_{j+1}^\dagger c_j) + h \sum_{j=1}^{L} \left(\prod_{i=1}^{j} \left(2c_i^\dagger c_i - 1 \right) \right) \right]. \tag{21}$$

In this form, the fermions represent the domain walls, and we can read off that the hopping strength of the domain wall is $(g-J)$ while the kink number violation term comes with the strength $(g+J)$.
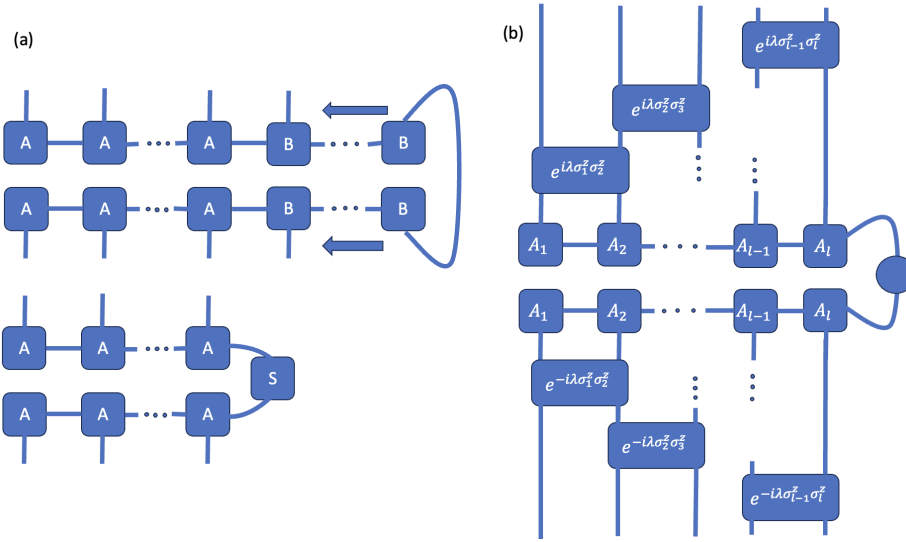
Figure 13: (a) The order of contraction of the legs of the tensor of the MPS wave function in the construction of the reduced density matrix $\rho_A = \text{Tr}_B(|\psi_{MPS}\rangle\langle\psi_{MPS}|)$ is shown in the arrow. (b)The MPO operators $e^{\pm i\lambda Q} = \prod_{i=1}^{l} e^{\pm i\lambda \sigma_i^z}$ (in site-type symmetry resolved entropy), and (c) The MPO operators $e^{\pm i\lambda Q} = \prod_{i=1}^{l-1} e^{\pm i\lambda \sigma_i^z \sigma_{i+1}^z}$ (in link-type symmetry resolved entropy) are applied successively via the DMRG algorithm. If the integral is split into $k+1$ steps, λ takes discrete values in the interval $[-2\pi, 2\pi]$ and this calculation is done for $(k+1)$ different λ before the Trapezoid Rule is applied to obtain $\rho_{A,Q}$
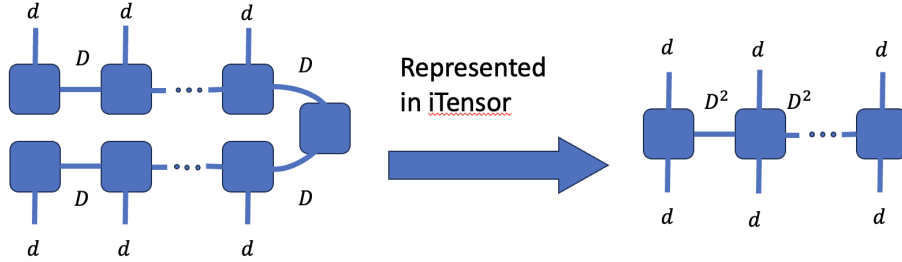

Figure 14: In iTensor, taking an outer product of an MPS $|\psi\rangle$ with itself (with bond dimension D) automatically forms an MPO density matrix with bond dimensions D^2.

F   Upper bound on Rényi Entropy for $h=0$ and kink-number preservation.

In this appendix, we prove that starting with a domain wall, and evolving with our Hamiltonian with $J = -g$ and $h = 0$ the second order half chain Rényi entropy $S_2 = -\log_2(\text{Tr}(\rho_A^2))$ is bound by 2 at all times. Concretely, we consider an initial state of the form:

$$|\psi(0)\rangle = |\uparrow ... \uparrow\downarrow_x ... \downarrow_{y-1}\uparrow_y ... \uparrow\rangle \tag{22}$$

To compute the evolution, we first apply the Kramers-Wannier U_{KW}, mapping the state to:

$$U_{\text{KW}}|\psi(0)\rangle = |1...(-1)_x 111(-1)_y 11 ...1\rangle. \tag{23}$$

Via a Jordan Wigner transformation this state will become the two particle state

$$U_{\text{KW}}|\psi(0)\rangle = c_x^\dagger c_y^\dagger |\text{vac}\rangle. \tag{24}$$

As explained above, the evolution of the state in the Jordan-Wigner picture is governed by the quadratic fermion Hamiltonian (21). In particular, when $g = -J$, the Hamiltonian does not involve pair creation terms. Under such
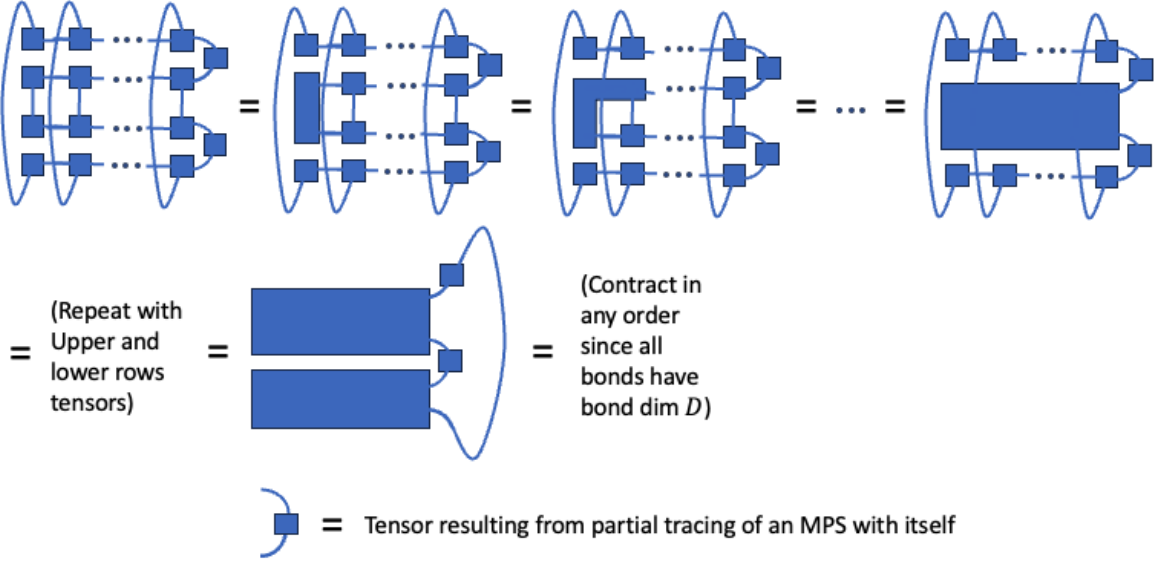
Figure 15: Minimal contraction order for individual tensors to compute $\mathrm{Tr}(e^{i\lambda Q}\rho_A e^{-i\lambda Q}\rho_A)$. Here the top 2 and bottom 2 rows of tensors can come from different reduced density matrix. The strategy for implementation here is to perform contractions of individual tensor component in MPS wave functions without first forming the density matrix MPOs, and the size tensor from partial trace can also be formed partial inner product of MPS wave function with itself.
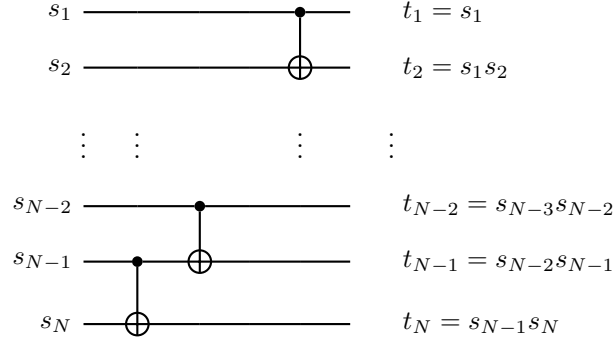

Figure 16: This quantum circuit implements the Kramers-Wannier Unitary on an open Ising spin chain.

evolution, the creation operators in (24) transform as:

$$c_\alpha^\dagger \longrightarrow \Sigma_j u_{\alpha\mathrm{j}} c_j^\dagger \tag{25}$$

with a unitary $L \times L$ matrix u. Therefore the evolved state is of the form:

$$U_{\mathrm{KW}}|\psi(t)\rangle = \Sigma_{i,j} u_{\mathrm{xi}} u_{\mathrm{yj}} c_i^\dagger c_j^\dagger |\mathrm{vac}\rangle = \Sigma_{i<j}\left(u_{\mathrm{xi}} u_{\mathrm{yj}} - u_{\mathrm{xj}} u_{\mathrm{yi}}\right) c_i^\dagger c_j^\dagger |\mathrm{vac}\rangle \tag{26}$$

We now undo the Kramers-Wannier transformation to get:

$$|\psi(t)\rangle = \Sigma_{i<j}\left(u_{\mathrm{xi}} u_{\mathrm{yj}} - u_{\mathrm{xj}} u_{\mathrm{yi}}\right)|\uparrow \ldots \uparrow\downarrow_i \ldots \downarrow_{j-1}\uparrow_j \ldots \uparrow\rangle \tag{27}$$

We now proceed by bounding the Schmidt rank of the state (27). We expand the summation explicitly as:

$$
\begin{aligned}
|\psi(t)\rangle &= \Sigma_{i\leq L_A}\Sigma_{j>L_A}\left(u_{\mathrm{x}i}u_{\mathrm{y}j}-u_{\mathrm{x}j}u_{\mathrm{y}i}\right)|\uparrow \dots \uparrow\downarrow_i \dots \downarrow_{j-1}\uparrow_j \dots \uparrow_N\rangle \\
&+ \Sigma_{i>L_A}\Sigma_{j>i}\left(u_{\mathrm{x}i}u_{\mathrm{y}j}-u_{\mathrm{x}j}u_{\mathrm{y}i}\right)|\uparrow \dots \uparrow\downarrow_i \dots \downarrow_{j-1}\uparrow_j \dots \uparrow_N\rangle \\
&+ \Sigma_{i<j}\Sigma_{j\leq L_A}\left(u_{\mathrm{x}i}u_{\mathrm{y}j}-u_{\mathrm{x}j}u_{\mathrm{y}i}\right)|\uparrow \dots \uparrow\downarrow_i \dots \downarrow_{j-1}\uparrow_j \dots \uparrow_N\rangle \\
&= \left(\Sigma_{i\leq L_A}u_{\mathrm{x}i}|\uparrow \dots \uparrow\downarrow_i \dots \downarrow_{L_A}\rangle\right)\otimes\left(\Sigma_{j>L_A}u_{\mathrm{y}j}|\downarrow_{L_A+1} \dots \downarrow_{j-1}\uparrow_j \dots \uparrow_N\rangle\right) \\
&- \left(\Sigma_{i\leq L_A}u_{\mathrm{x}j}|\uparrow \dots \uparrow\downarrow_i \dots \downarrow_{L_A}\rangle\right)\otimes\left(\Sigma_{j>L_A}u_{\mathrm{y}i}|\downarrow_{L_A+1} \dots \downarrow_{j-1}\uparrow_j \dots \uparrow_N\rangle\right) \\
&+ |\uparrow \dots \uparrow\uparrow_{L_A}\rangle\otimes\left(\Sigma_{i>L_A}\Sigma_{j>i}\left(u_{\mathrm{x}i}u_{\mathrm{y}j}-u_{\mathrm{x}j}u_{\mathrm{y}i}\right)|\uparrow \dots \uparrow\downarrow_i \dots \downarrow_{j-1}\uparrow_j \dots \uparrow_N\rangle\right) \\
&+ \left(\Sigma_{i<j}\Sigma_{j\leq L_A}\left(u_{\mathrm{x}i}u_{\mathrm{y}j}-u_{\mathrm{x}j}u_{\mathrm{y}i}\right)|\uparrow \dots \uparrow\downarrow_i \dots \downarrow_{j-1}\uparrow_j \dots \uparrow_{L_A}\rangle\right)\otimes|\uparrow \dots \uparrow\uparrow_N\rangle.
\end{aligned}
\tag{28}
$$

Observe that in the last line we have explicitly separated $|\psi(t)\rangle$ into a combination of the form:

$$
|\psi(t)\rangle = \Sigma_{\alpha=1}^4|\phi_\alpha\rangle\otimes|\tilde{\phi}_\alpha\rangle.
\tag{29}
$$

Note that for the rest of the argument, it doesn't matter if $\phi_\alpha,\tilde{\phi}_\alpha$, are normalized or represent orthogonal sets. Indeed, the form (29) immediately implies that the Schmidt rank of the state $|\psi(t)\rangle$ with respect to this partition is at most $\mathrm{Sch}(\psi(t)) \leq 4$ (see Problem 2.2 in [47]). Since the logarithm of the Schmidt number is a bound on entropy (Von Neumann entropy, and as consequence also Rényi entropy) we have that:

$$
S_2 \leq \log_2 \mathrm{Sch}(\psi(t)) \leq \log_2 4 = 2.
\tag{30}
$$

Accepted in 〈 〉uantum 2024-08-21, click title to verify. Published under CC-BY 4.0.

21